The transport of sediment mixtures examined with a birth-death model for grain-size fractions

Shawn M. Chartrand[1,3] and David Jon Furbish[1,2]

[1]Department of Earth and Environmental Science, Vanderbilt University, Nashville, TN, USA
[2]Department of Civil and Environmental Engineering, Vanderbilt University, Nashville, TN, USA
[3]Now at Department of Environmental Science, Simon Fraser University, Burnaby, BC, Canada

Correspondence: Shawn M. Chartrand (shawn_chartrand@sfu.ca)

Abstract. Bedload transport of sediment mixtures in mountain streams is challenging to predict, with implications for understanding how rivers form and respond to environmental change. Experimental work shows that collective particle entrainment is an important contributing mechanism of bedload transport, but questions remain. We use four different time series of experimental sediment flux for granular particles 4–32 mm in diameter to indirectly examine the role of collective mobilization.

5   Flux was measured at a fixed position in space using an imaging light table. The light table provides a flux measurement that is sampled at a resolution of 1 Hz, and for total time durations ranging from 75 to 240 min. Experimental conditions include periods of statistical steady-state, and transient adjustments due to changes of the upstream supply of water and sediment. We find that despite the contrasting experimental conditions, the time series encode a consistent transport behaviour within the Fourier domain: the transport of finer grain size populations has increasing power density for decreasing frequency, whereas

10 the transport of larger grain size populations has a near constant power density across all frequencies. Hence, smaller particle sizes dominate the power spectra. We seek an explanation for this result, and elaborate on a probabilistic birth-death model introduced to the field by Christophe Ancey and colleagues. Analysis using the expanded birth-death model provides two important results. The transport of smaller particles includes collective entrainment terms that represent grain mobilization due to smaller and larger particle sizes colliding with the streambed surface. In contrast, the transport of larger particles includes

15 collective entrainment terms limited to larger particle sizes. The size-dependent collective controls on particle mobilization is an important finding, and we show that it offers a testable explanation for observed flux differences between smaller and larger particle sizes, common to gravel-bed mountain streams. As a result, our work motivates the need to better understand collective entrainment within the context of granular sediment transport along mountain stream beds.

1   Introduction

20 This is a concept paper that examines how collective entrainment contributes to the transport of sediment mixtures in rivers. Collective entrainment initiates the downstream motion of two or more bedload particles in close proximity, and at roughly the same time. The mechanisms of collective particle entrainment relate to fluid phenomena (Drake et al., 1988), bed surface particle arrangements (Böhm et al., 2004), and moving grains that impact the bed (Ancey et al., 2008; Ancey, 2010; Lee and Jerolmack, 2018). The combined effect of these mechanisms yields a time varying flux of bedload particles, when observed

at a fixed position. Particle flux variations occur at time scales of seconds, to tens of seconds and longer, and relatively large variations are a hallmark of a stochastic process. Our primary goal here is to learn more about controls on fluctuations of bedload transport using time series of sediment flux in an experimental flume.

Einstein (1937) proposed that the movement of bedload particles along a river bed is a probabilistic problem. He noted

5 that particles of similar size released into an experimental flume at the same instant in time traveled different distances. An implication of this finding is that bedload transport kinematics (i.e., particle travel distances and rates of motion) are specified by probability distributions, rather than by unique values. This insight motivates more recent work aimed at developing a theory of sediment transport as a probabilistic phenomenon. The development of probabilistic bedload transport theory is informed by physical and numerical experiments (Einstein, 1937; Wiberg and Smith, 1987; Ancey et al., 2006, 2008; Ancey, 2010;

10 Lajeunesse et al., 2010; Furbish et al., 2012a, b; Roseberry et al., 2012; Fathel et al., 2015; Furbish et al., 2016, 2017, e.g.). A tenet of this work is that the entrainment or mobility of particles resting on a river bed is a stochastic process, with distributions of travel distances and inter-travel period resting times (see Einstein, 1937; Hassan et al., 1991). Consequently, the number of moving particles per unit area of the bed, and the particle motion components of travel time, travel distance and downstream average velocity are characterized by probability distributions with right tails (Hubbell and Sayre, 1964; Hassan et al., 1991;

15 Lajeunesse et al., 2010; Furbish et al., 2012b; Roseberry et al., 2012; Fathel et al., 2015).

Experimental observations of particle motions have typically involved tracking grains moving within an image reference area. Here we ask what can be learned from the analogous case of measuring sediment flux at a fixed position in space, at a high temporal resolution and for a period of time that is long relative to particle travel times of fractions or a few seconds or more (e.g. Drake et al., 1988; Roseberry et al., 2012; Fathel et al., 2015). More specifically, what do near-continuous time

20 series of sediment flux reveal about the transport of sediment mixtures? We know of only a limited number of studies that have reported and analyzed near-continuous measurements of sediment flux at a fixed position, and for time scales that range from minutes to hundreds of hours (e.g. Frey et al., 2003; Zimmermann et al., 2008; Singh et al., 2009; Jerolmack and Paola, 2010; Turowski et al., 2011; Ferrer-Boix and Hassan, 2015; Saletti et al., 2015; Dhont and Ancey, 2018; Lee and Jerolmack, 2018; Phillips et al., 2018; Redolfi et al., 2018; Masteller et al., 2019).

25 Dhont and Ancey (2018) analyze a long time series of sediment flux data from a flume outlet. Their experimental design emphasized the examination of how bed morphology affects sediment transport under steady conditions of upstream sediment supply. Their experimental duration was approximately 550 h, during which sediment output from the flume was averaged over periods of 1 min. Sediment flux shows variations that span several orders of magnitude around the sediment supply rate. Dhont and Ancey (2018) report that excursions above the supply rate were typified by pulses which rise to a maximum

30 value over relatively short time intervals. The intermittent sharp increases of sediment flux within the time series results in a visually erratic signal (Singh et al., 2009). However, the flux power spectrum suggests order within the signal, notably that flux variations with frequencies f between $10^{-4.8}$ to 10^{-2} Hz fall off as $f^{-3/2}$ Hz. Dhont and Ancey (2018) indicate that the lower frequency $10^{-4.8}$ Hz flux component corresponds to the approximate arrival of migrating bars, leading to a majority of the measured peak bedload transport rates. The higher frequency flux variations occur within the bar inter-arrival times. The

35 fall off slope of the calculated flux power spectrum reported by Dhont and Ancey (2018) is a striking result of their work. The

authors did not provide an explanation for possible controls on the spectra fall off slope. As we discuss below, this behaviour is a primary focus of our work.

Saletti et al. (2015) take a different approach and use 13 sediment sampling intervals lasting 10 min to evaluate sediment transport dynamics from an experimental step-pool channel. Sediment flux measured at the flume outlet was the outcome of

5　channel adjustment in the absence of upstream sediment supply, coupled with a stepped hydrograph marked by periods of steady water supply. The authors consider sediment flux as an autocorrelated phenomenon, and show that the Hurst exponent (H) exhibits dependence on the sediment flux magnitude and grain size. The reported experimental conditions of larger flux magnitudes and finer flux compositions have $H \rightarrow 1$, whereas smaller flux magnitudes and coarser compositions have $H \rightarrow 0.5$. These results imply that the transport of finer sediments upstream of the flux measurement point is more continuous in time

10　and space (also see Kuhnle and Southard, 1988). This contrasts with the transport of coarser particles, which by comparison is more intermittent. Saletti et al. (2015) attribute the different flux responses to the time varying magnitude of upstream bed slope adjustment.

Lee and Jerolmack (2018) report results from a series of experiments designed to examine how bedload transport responds to changes in the driving frequency of transport, controlled by different sediment supply rates to a small flume. High-speed

15　imaging of particle motions shows that entrainment of marbles occurs through collisions of moving particles with the bed surface, generally setting two or more marbles into collective motion. The total displacement distance of marbles, and the mean number of marbles set into motion scales in a linear way with the total kinetic energy transferred to surface particles by colliding marbles. However, entrainment of a given number of marbles is shown to be described by a distribution of total kinetic energies, suggesting that entrainment depends on numerous local conditions, which are difficult to anticipate. Related

20　to our work here, Lee and Jerolmack (2018) provide clear evidence that collective entrainment is an important physical process of bedload transport. This finding links directly with theoretical work by Ancey et al. (2008) and Ancey (2010) who develop a stochastic model of bedload transport that explicitly accounts for collective particle entrainment.

Here, we build upon the work of Ancey et al. (2008) and Ancey (2010), as elaborated by Heyman (2014) and Heyman et al. (2014), Saletti et al. (2015) and Dhont and Ancey (2018), and examine sediment transport through the information embedded

25　within an experimental particle flux time series of two contrasting conditions: steady-state followed by a transient. In our work, steady-state is defined by two different conditions for periods of time much greater than time averaged particle travel times: (1) the sediment supply rate is comparable to the flux, and (2) changes to the mean bed elevation approaches zero. In contrast, a transient state is characterized by relatively large negative differences between the rate of sediment supply and flux, therefore the channel profile undergoes rapid changes. Our focus is important because the time varying character of sediment flux yields

30　specific information about the upstream bedload transport process. Furthermore, an examination of flux time series between steady-state and transient conditions permits us to explore whether bedload transport processes depend on the adjustment state of upstream areas of the river bed which contribute directly to the measured flux. Furthermore, our experiments include initial and repeat phases, providing for a comparison of flux between specifically two sets of overall similar conditions.

We address several questions. First, are all grain size fractions transported at similar rates determined by time averaged

35　counts of moving particles? It is generally accepted that the relative proportion of grain sizes present on the bed surface will
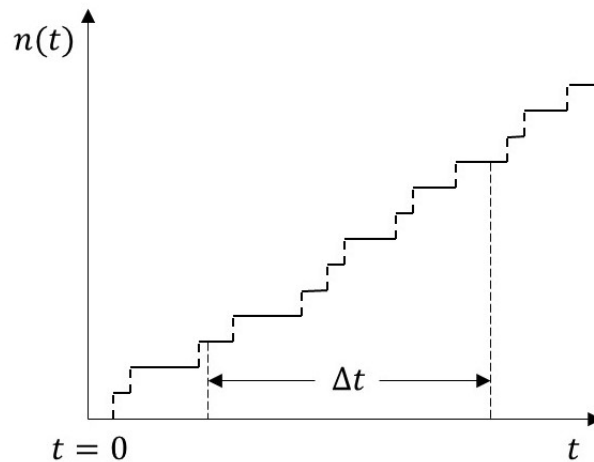
Figure 1. Definition diagram for the number of particles $n(t)$ exiting the right boundary of an area A during an interval Δt.

influence the overall flux magnitude for each particular size class (e.g. Parker, 1990; Wilcock and McArdell, 1997; Wilcock and Crowe, 2003). However, are effects related to grain size proportion evident in the time series signal of grain size specific flux? Second, do statistical steady-state and transient sediment signals carry the same information about the transport process? That is, other than possible differences in flux magnitude, can we specifically infer from flux data if the bedload transport process

5 is similar, or differs between steady-state and transient? Third, the transport process information encoded within sediment flux time series can be understood through power spectral analysis. Jerolmack and Paola (2010) and Dhont and Ancey (2018) show that the power spectra of total flux can exhibit, for example, power law structure over a finite frequency band or time scale range. What transport mechanisms are responsible for the spectral structure?

We use time series analysis to explore these questions, and we expand the Markov birth-death framework of Ancey et al.

10 (2008) and Ancey (2010) to particle size mixtures. Our work provides further evidence that sediment mixtures exhibit size-dependent transport at low to moderate rates of particle flux. Power spectra for steady-state and transient conditions indicate that fine grain flux is dominated by frequencies less than approximately f^{-2} Hz. In contrast, coarse particle flux shows no dominant frequency or frequency band, reflecting a white noise bedload transport process. We show that the fine grain flux spectra likely reflects the effects of collective entrainment in the birth-death model, which accounts for larger grains collectively entraining

15 finer ones. This collective effect diminishes with grain size as the pool of particles capable of setting larger grains into motion is presumed to decrease. Our combined results further motivates the critical need for continued development of a probabilistic theory of sediment transport for gravel-bed rivers. Fruitful next steps include an emphasis on further examination of the physical controls of collective particle entrainment. The recent work by Lee and Jerolmack (2018) offers one experimental basis from which future work can move forward.
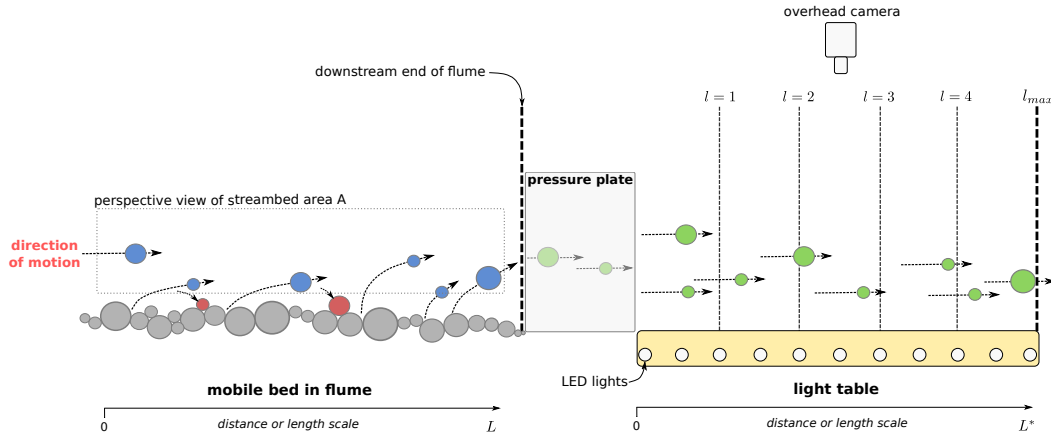
Figure 2. Definition diagram of a light table system within which the sediment particle flux is measured downstream of a flume (see Zimmermann et al., 2008; Chartrand et al., 2018). The vertical dashed gray lines over the light table mark 5 sub-regions of the light table within which particle flux is estimated using successive images of the light table (15–20 Hz).

2 Problem Set-up

Our work explores the time dependent character of grain-size specific sediment flux measured in the laboratory during development and adjustment of pool-riffle like bed topography (see Chartrand et al., 2018). Since sediment flux is measured in a variety of ways in the laboratory (e.g. Frey et al., 2003; Zimmermann et al., 2008; Singh et al., 2009) and the field (e.g. Hubbell, 1964; Helley and Smith, 1971; Diplas et al., 2008; Rickenmann, 2018), it is important to establish context for the information carried by the transport time series that we report here (cf. Heyman et al., 2013).

2.1 Particle Activity

Consider an idealized streambed area A with streamwise length L and width B. Particles enter A through the left boundary and exit through the right boundary. Neither entrainment nor deposition occurs within A. At any time t there are $N(t)$ moving particles within A and the associated particle number activity is $\gamma(t) = N(t)/A$.

Let $n(t)$ denote the number of particles of a given size that exits the right boundary following an arbitrary starting time $t = 0$ (Fig. 1). The number discharge specific to a measurement interval Δt is then

$$Q_{\Delta t}(t) = \frac{n(t + \Delta t) - n(t)}{\Delta t} = \frac{\Delta n}{\Delta t}, \tag{1}$$

where for convenience we associate this finite difference with time t. Because $n(t)$ is a stepped function of time, the limit of the right side of Eq. (1) as $\Delta t \to 0$ is strictly zero or undefined. Thus $Q_{\Delta t}$ represents an average discharge over the interval Δt.

Consider the light table configuration described by Zimmermann et al. (2008) (Fig. 2). Particles that leave the upstream flume travel under a pressure plate, and cross the light table at approximately constant velocity. Processing of five successive images (15–20 Hz) as particles cross the table leads to an estimate of the number of particles of each size fraction that crosses

the downstream boundary of the table during successive time intervals. This is equivalent to the numerator Δn on the right side of Eq. (1).

If between time t and time $t + \Delta t$ a number of particles, Δn, crossed the downstream boundary of the light table, then assuming a constant particle velocity u_p^* over the table, this number of particles resided on the light table within some area A^*

5   at time t. At this instant the particle activity associated with A^* is $\gamma^*(t) = \Delta n / A^*$. That is, upon setting $\Delta n = N(t)$, this is the activity $\gamma^*(t) = N(t)/A^*$ on the light table, although A^* may differ from the actual area of the apparatus.

The vertically integrated flux is $q_{\Delta t}(t) = Q_{\Delta t}(t)/B^*$. This implies that $q_{\Delta t}(t) = \gamma^*(t)L^*/\Delta t$. Setting $u_p^* = L^*/\Delta t$ then gives

$$q_{\Delta t}(t) = \gamma^*(t)u_p^*, \tag{2}$$

10   where L^* now must be interpreted as the distance traveled by particles over the light table at velocity u_p^* during the interval Δt.

The number of particles Δn that cross the right boundary of the light table during Δt and which resided on the light table at time t were delivered from upstream across the left boundary of the light table (Fig. 2). By continuity, this influx across the left boundary is equal to that expressed in Eq. (2), but it occurred during an interval Δt prior to time t. By an argument similar to that above, we can envision a streambed area A contributing to this flux equal to

15   $$q_{\Delta t} = \gamma \overline{u}_p, \tag{3}$$

where γ is the number activity associated with A and $\overline{u}_p$ is the average particle velocity. If variations in the velocities of a given size are small, then the distance L is interpreted as the distance traveled by particles over the streambed at velocity $\overline{u}_p$ during Δt. Moreover, if we momentarily assume that the difference between entrainment and deposition within A during Δt is negligible, then

20   $$\gamma \approx \frac{u_p^*}{\overline{u}_p}\gamma^* = \frac{q_{\Delta t}}{\overline{u}_p}. \tag{4}$$

That is, the particle number activity within the streambed area A upstream from the light table is directly proportional to that measured on the light table, albeit separated in time by at least Δt.

In fact, entrainment and deposition within an area A are not likely to be balanced during Δt. What is important is that the activity γ^* is a measure of the upstream activity in Eq. (3) of particles delivered to the light table. Our association of upstream

25   activity and flux measured by the light table is an important assumption of our expanded birth-death formulation, which we now present.

2.2   Birth-Death Formulation

Following Ancey (2010), for a specified streambed area A (Fig. 2), the number of active particles of the jth size class may be expressed as

30   $$\frac{\partial n_j(t)}{\partial t} = v_j + \lambda_j + \mu_j n_j - \sigma_j n_j - w_j n_j \tag{5}$$

Here, v_j is the immigration rate, λ_j is the entrainment rate normally attributed to fluid forces, μ_j is a rate constant of collective entrainment, σ_j is a rate constant of deposition, and w_j is a rate constant of emigration. To be clear, the fluid related entrainment rate is viewed as dislodgement from the bed due to fluid forces, as in the classic assumption in sediment transport (e.g. Shields, 1936; Meyer-Peter and Muller, 1948). Collective entrainment is viewed as dislodgement "because of the moving particles,

5   which can interact directly (collision) or indirectly (wake effect, advection of turbulent structure) with the bed particles" (Ancey, 2010). To this we add the possibility that entrainment of a particle from the bed leads to the onset of motion of nearby particles with localized rearrangement and destabilization of the bed (Böhm et al., 2004; Lee and Jerolmack, 2018; Chartrand, 2017).

Letting a circumflex denote a Fourier transform, the birth-death formulation, Eq. (5), is represented in the frequency domain
10   as:

$$i\omega\hat{n}_j = \hat{v}_j + \hat{\lambda}_j + \mu_j\hat{n}_j - \sigma_j\hat{n}_j - w_j\hat{n}_j, \qquad (6)$$

where $\omega = 2\pi/T$ is the angular frequency with period T. For a specified area A, the immigration rate v_j and the emigration rate $w_j n_j$ may differ at any instant. However, because the emigration rate for any area A is just the immigration rate for the downstream area, the spectra of these must be the same for statistically uniform transport. This means that $\hat{v}_j = w_j\hat{n}_j$, and we
15   rewrite Eq. (6) (see Appendix D):

$$i\omega\hat{n}_j = \hat{\lambda}_j + \mu_j\hat{n}_j - \sigma_j\hat{n}_j. \qquad (7)$$

Rearranging Eq. (7) provides the grain size specific Fourier transform of the number of active particles for a specified streambed area A (Fig. 2):

$$\hat{n}_j = \frac{1}{(\sigma_j - \mu_j) + i\omega}\hat{\lambda}_j. \qquad (8)$$

20   The Fourier transformed particle activity $\hat{n}_j$ is determined by the ratio of two different physical affects. First, $\hat{n}_j$ depends directly on the fluid entrainment rates across the frequencies $i\omega$. For example, at low to moderate bedload transport stages (Hassan et al., 2005), particle entrainment frequencies due to the time-averaged downstream fluid velocity versus that due to turbulent sweeps of fluid at the bed differs. The former produces fluid entrainment of particles at frequencies that are high relative to turbulent sweeps, which occur at some characteristic time scale (Ancey et al., 2008; Singh et al., 2009).
25   Second, $\hat{n}_j$ depends inversely on the balance between particle deposition and collective entrainment rate constants, which can attenuate or amplify $\hat{\lambda}_j$. In general, $\hat{\lambda}_j$ is amplified at times when deposition and collective entrainment are comparable, and is attenuated when deposition is large relative to collective entrainment, assuming $\mu_j \lesssim \sigma_j$ (e.g. Ancey, 2010; Heyman et al., 2014). However, the amplification or attenuation effect to $\hat{\lambda}_j$ is influenced further by the range of frequencies $i\omega$ of bedload transport in gravel-bed rivers. As a result, regardless of whether $\hat{\lambda}_j$ is amplified or attenuated by $(\sigma_j - \mu_j)^{-1}$, the sum acts
30   as a low pass filter on $\hat{\lambda}_j$. Physically, this result indicates that bedload transport is characterized by relatively high frequency fluctuations (e.g. Ancey et al., 2006; Jerolmack and Paola, 2010; Fathel et al., 2015). We discuss these issues in more detail below following further development of the birth-death model.
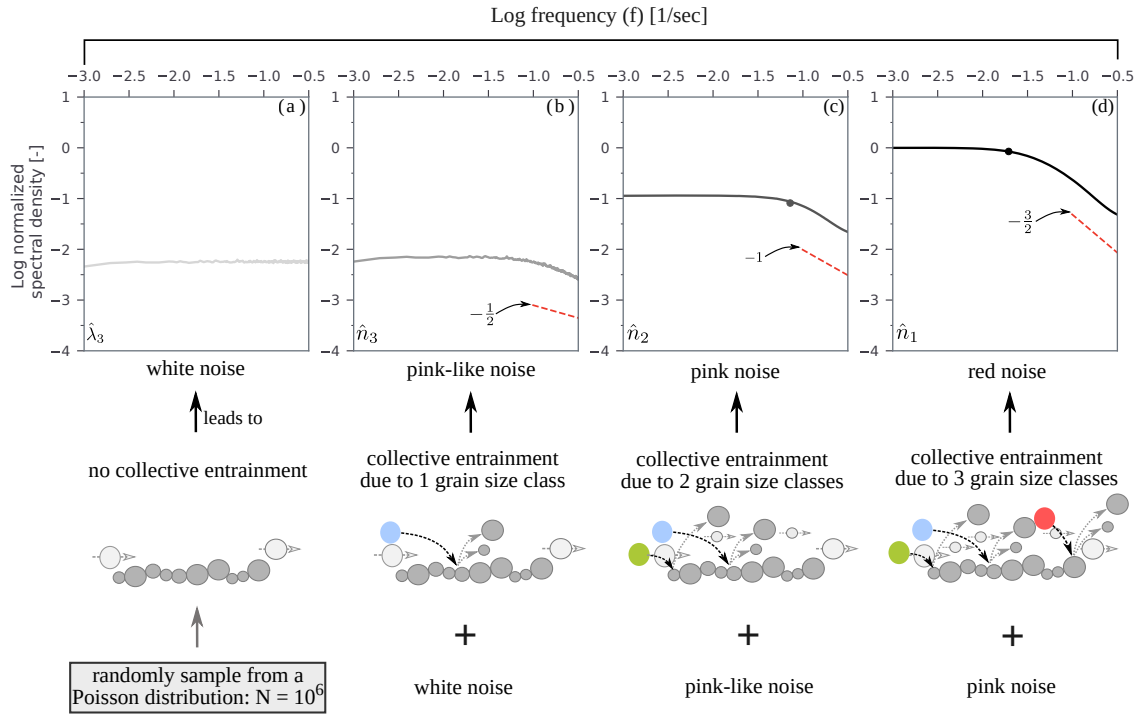
Figure 3. Example of how an input white noise for n_3 contributes to a red noise signal for n_1 based on our imagined 3 particle size system, and over the frequency band 10^{-3} to $10^{-0.5}$ Hz. The power spectral density of (a) is based on randomly sampling a Poisson distribution 10^6 times; (b) results from setting λ_3 of Eq. (18) equal to the white noise signal of (a); (c) calculating Eq. (19); and (d) calculating Eq. (20). Parameter values for Eqs. (18)–(20) are: ϕ_{aj}, $\phi_{bj} = 0.1$; σ_1–$\sigma_3 = 1.0$, μ_{33}, μ_{22} and $\mu_{21} = 0.2$; and μ_{31}, μ_{21} and $\mu_{11} = 0.8$. All power spectral densities are normalized by the maximum power of (d) for plotting and comparison. The red dashed curves in (b)-(d) indicate $1/f^{-n}$ fall off behaviour, and the circles plotted on top of each curve in (b)–(d) are the inflection points.

Expanding on Eq. (5), consider three particle size classes ($j = 1, 2, 3$), small to large. For simplicity, assume that collective entrainment of the jth size involves the jth and larger sizes:

$$\frac{\mathrm{d}n_3}{\mathrm{d}t} = \lambda_3 + \mu_{33}n_3 - \sigma_3 n_3, \tag{9}$$

5 $$\frac{\mathrm{d}n_2}{\mathrm{d}t} = \lambda_2 + \mu_{22}n_2 + \mu_{32}n_3 - \sigma_2 n_2, \text{ and} \tag{10}$$

$$\frac{\mathrm{d}n_1}{\mathrm{d}t} = \lambda_1 + \mu_{11}n_1 + \mu_{21}n_2 + \mu_{31}n_3 - \sigma_1 n_1. \tag{11}$$

The first subscript on the collective entrainment rate constant μ denotes the influencing particle size and the second subscript denotes the influenced size. Taking the Fourier transforms,

$$i\omega\hat{n}_3 = \hat{\lambda}_3 + \mu_{33}\hat{n}_3 - \sigma_3\hat{n}_3, \tag{12}$$

5    $$i\omega\hat{n}_2 = \hat{\lambda}_2 + \mu_{32}\hat{n}_3 + \mu_{22}\hat{n}_2 - \sigma_2\hat{n}_2, \text{ and} \tag{13}$$

$$i\omega\hat{n}_1 = \hat{\lambda}_1 + \mu_{31}\hat{n}_3 + \mu_{21}\hat{n}_2 + \mu_{11}\hat{n}_1 - \sigma_1\hat{n}_1. \tag{14}$$

Rearranging then leads to:

$$\hat{n}_3 = \frac{1}{(\sigma_3 - \mu_{33}) + i\omega}(\hat{\lambda}_3), \tag{15}$$

10

$$\hat{n}_2 = \frac{1}{(\sigma_2 - \mu_{22}) + i\omega}(\hat{\lambda}_2 + \mu_{32}\hat{n}_3), \text{ and} \tag{16}$$

$$\hat{n}_1 = \frac{1}{(\sigma_1 - \mu_{11}) + i\omega}(\hat{\lambda}_1 + \mu_{31}\hat{n}_3 + \mu_{21}\hat{n}_2). \tag{17}$$

Equations 15–17 indicate that the spectrum of the *j*th size involves the sum of the spectra of coarser sizes, each modified by a

15   low-pass filter of the same form, i.e. $1/[\sigma_j - \mu_{ii} + i\omega]$. We simplify the notation and use F_j to represent the low pass filters:
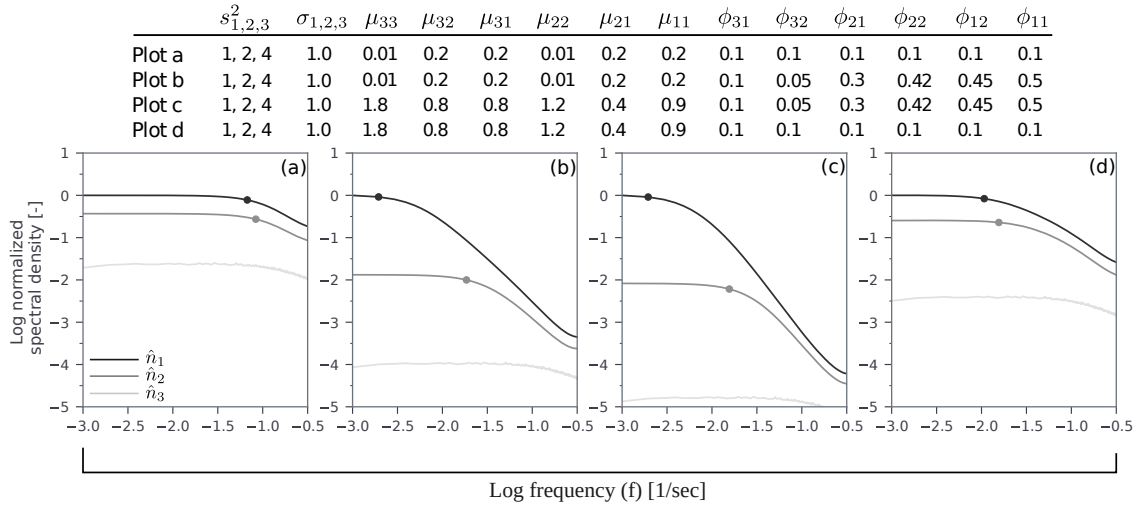
$$\hat{n}_3 = F_3(\omega)(\hat{\lambda}_3), \tag{18}$$

$$\hat{n}_2 = F_2(\omega)(\hat{\lambda}_2 + \mu_{32}\hat{n}_3), \text{ and} \tag{19}$$

20    $$\hat{n}_1 = F_1(\omega)(\hat{\lambda}_1 + \mu_{31}\hat{n}_3 + \mu_{21}\hat{n}_2). \tag{20}$$

In order to solve Eqs. (18–20) and learn about the three particle size birth-death model, we need to complete two last steps. First, we find the real part of the low pass filters $\mathrm{Re}(F_j)$ (see Appendix D):

$$\mathrm{Re}(F_3[\omega]) = \frac{1}{\sqrt{(\sigma_3 - \mu_{33})^2 + \omega^2}}, \tag{21}$$

Earth **Surface**
Dynamics
Discussions

	$s^2_{1,2,3}$	$\sigma_{1,2,3}$	μ_{33}	μ_{32}	μ_{31}	μ_{22}	μ_{21}	μ_{11}	ϕ_{31}	ϕ_{32}	ϕ_{21}	ϕ_{22}	ϕ_{12}	ϕ_{11}
Plot a	1, 2, 4	1.0	0.01	0.2	0.2	0.01	0.2	0.2	0.1	0.1	0.1	0.1	0.1	0.1
Plot b	1, 2, 4	1.0	0.01	0.2	0.2	0.01	0.2	0.2	0.1	0.05	0.3	0.42	0.45	0.5
Plot c	1, 2, 4	1.0	1.8	0.8	0.8	1.2	0.4	0.9	0.1	0.05	0.3	0.42	0.45	0.5
Plot d	1, 2, 4	1.0	1.8	0.8	0.8	1.2	0.4	0.9	0.1	0.1	0.1	0.1	0.1	0.1

Figure 4. Equations (15)–(17) calculated for a range of conditions over the frequency band 10^{-3} to $10^{-0.5}$ Hz, and based on a white noise input signal for λ_3 in all cases. The different parameter values used for the calculations shown in each subplot are given in the table above the Figure. The circles plotted on top of each curve tracks how the inflection point for each spectrum shifts toward lower frequencies, depending on specific values used for each term of Eqs. (15)–(17).

$$\mathrm{Re}(F_2[\omega]) = \frac{1}{\sqrt{(\sigma_2 - \mu_{22})^2 + \omega^2}}, \text{ and} \tag{22}$$

$$\mathrm{Re}(F_1[\omega]) = \frac{1}{\sqrt{(\sigma_1 - \mu_{11})^2 + \omega^2}}. \tag{23}$$

5   Next, we need to specify or calculate the Fourier transform of the time varying fluid entrainment signals for each particle size $\hat{\lambda}_j$, Eq. (5) and Eqs. (18–20). Based on experimental evidence, we assume the largest grain size class $\hat{\lambda}_3$ is a white noise (Saletti et al., 2015). On the other hand, transport of the two smaller grain size classes $\hat{\lambda}_2$ and $\hat{\lambda}_1$ is assumed to follow an autoregressive process, and specifically a second-order AR(2) process. An implication of our assumption is that the fluid entrainment rate of particles at time t is correlated to rates during the two previous times, and furthermore may carry longer term memory of prior particle entrainment events (Ancey et al., 2008; Saletti et al., 2015). The temporal correlation is likely stronger, however, for all but the weakest or most sporadic transport conditions (e.g. Drake et al., 1988; Ancey et al., 2008; Roseberry et al., 2012; Fathel et al., 2015; Saletti et al., 2015; Lee and Jerolmack, 2018). As a result, use of an AR(2) process to model $\hat{\lambda}_2$ and $\hat{\lambda}_1$ is at best illustrative of actual fluid entrainment conditions.

The power spectra for $\hat{\lambda}_2$ and $\hat{\lambda}_1$ of an AR(2) process is defined as (Box et al., 2008):

15   $$\hat{\lambda}_j = \frac{2s_j^2}{1 + \phi_{aj}^2 + \phi_{bj}^2 - 2\phi_{aj}(1 - \phi_{bj})A - 2\phi_{bj}B}, \tag{24}$$

where

$$A = cos(2\pi\omega), \text{ and} \tag{25a}$$

$$B = cos(4\pi\omega). \tag{25b}$$

The term s_j^2 is the variance of an input white noise process, ϕ_{aj} and ϕ_{bj} are the autoregressive model coefficients, which here have positive values due to the low-pass behaviour of Eq. (8). Equations (18–25b) along with values for ϕ_{aj}, ϕ_{bj} and μ_{jj} permit calculation of the flux power spectral densities $\hat{n}_1$–$\hat{n}_3$ for our exploratory three particle size system. To that end, we provide

5   two examples to illustrate the behaviour of the birth-death model presented above.

Based on Saletti et al. (2015), suppose that $\hat{\lambda}_3$ is a white noise measured at the upstream boundary of A (Figs. 2 and 3a). This signal is passed through the low-pass filter $F_3(\omega)$ (Eq. 18), resulting in pink-like noise structure for $\hat{n}_3$ (Fig. 3b). Next, $\hat{n}_3$ is modulated by μ_{32} (Eq. 19) and added to $\hat{\lambda}_2$. The resulting quantity is then passed through the low-pass filter $F_2(\omega)$ (Eq. 19), resulting in pink noise structure for $\hat{n}_2$ (Fig. 3c). The process continues and expands for the finest grain size (Eq. 20), and

10   results in red noise structure for $\hat{n}_1$ (Fig. 3d). So, even if $\hat{\lambda}_3$ is initially a white noise (Fig. 3a), the outcome for smaller grain size classes is a spectrum dominated by low frequencies (Figs. 3b–3d). In fact, because the same filtering process is occurring upstream, the signals $\hat{n}_1$ or $\hat{n}_2$ are unlikely to be white noise signals (Fig. 3). In this example we use unique values for each of the parameters of Eqs. (18)–(23), which raises the question how does the birth-death model for a mixture of three particle sizes behave under a broader set of parameter conditions?

15   Power spectra dominated by low frequencies for the two smaller particle sizes is achieved in at least two different ways using the birth-death model with a broader set of parameter values (Fig. 4). First, larger AR(2) weight parameters for the two smaller particle sizes amplifies and shifts power to increasingly lower frequencies as particle size decreases (compare Figs. 4a and 4b). A slightly more pronounced effect is achieved by further increasing collective entrainment for the smaller particle sizes relative to the largest size (compare Figs. 4b and 4c). Finally, amplification of the lower frequencies is reduced, but not

20   eliminated, when the AR(2) weight parameter values are decreased, revealing that collective entrainment can amplify lower frequency spectral power (compare Figs. 4a, 4c and 4d) (cf. Ancey and Heyman, 2014). These combined results suggest that lower frequency spectral power is amplified by enhanced effects due to local fluid driven entrainment, as well as collective entrainment (Ancey et al., 2008; Lee and Jerolmack, 2018). However, the amplifying effect of fluid entrainment may be more important. Regardless, more work is needed to better understand the numerical characteristics of terms in Eqs. (18–23) (Ancey

25   and Heyman, 2014).

Next, we review important details of an experiment which provides sediment flux time series arising from the transport of a grain size mixture. The time series provide an important empirical data set which we use to more carefully consider the exploratory birth-death model developed, described and illustrated in Figs. 3 and 4.
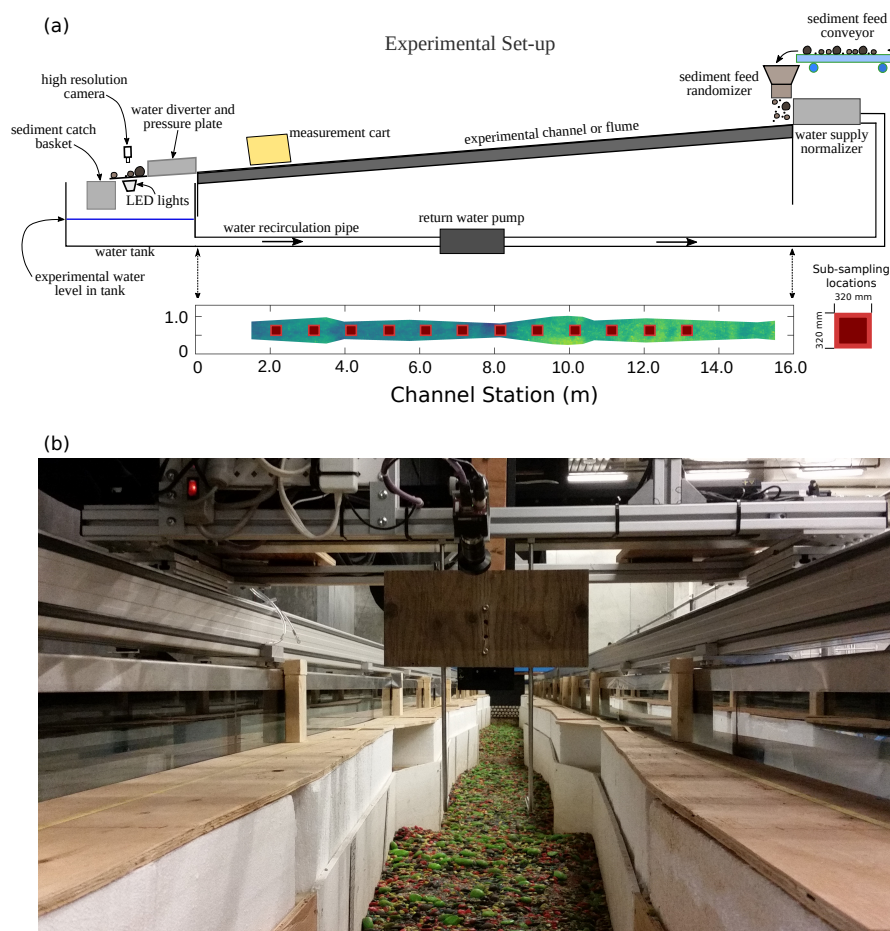
Figure 5. Graphical overview and image of the experimental setup. (a) Schematic illustration of the experimental setup, including an overhead view of the experimental channel, showing the downstream width variation and subsampling locations indicated by red boxes. (b) Photograph of the experimental channel. The photograph view is looking upstream from station 1500 mm. Photograph taken at experimental time 2150 min. Figure modified from Chartrand et al. (2018).

3   Methods

Experimental data reported here corresponds to pool-riffle experiment 1 (PRE1) conducted at the BioGeoMorphic eXperimental Laboratory (BGMX Lab) at the University of British Columbia, Vancouver, Canada. The experimental flume measures 16 m in total length and 1 m in width, and we use 15 m to conduct the experiments. Water recirculates through the flume via a pump, but sediment does not (Fig. 2). We introduce water to the upstream channel boundary through a series of stacked 5 cm diameter plastic pipes, collectively called the flow normalizer. The normalizer is 1 m in length, or roughly $2w'$ in length, where w' is the average channel width, and we use it to establish an initially uniform flow. We introduce sediment to the flume via a speed-controlled conveyor, which dumps particles into a mixing chamber we call the randomizer. The randomizer consists of
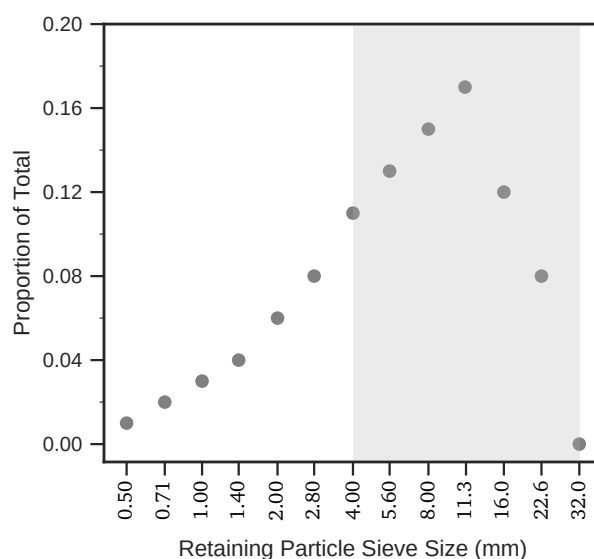
Figure 6. PRE1 experimental grain size distribution for the retaining sieve size shown on the x-axis. The x-axis is presented in log_{10} scale. The gray shaded region highlights the grain size classes reported here.

a vertical shaft with alternating cross-bars spanning the width of the shaft. As particles fall through the mixing chamber, their pathways are interrupted by the cross-bars, which flings the particles along random trajectories, providing a spatially-random distribution of sediment fall points on the inlet flume bed. The randomizer action provides a spatially and temporally uniform inlet boundary condition, which did not require manual adjustment during the experiments due to development of a sediment
5 pile at the flume inlet.

The flume outlet elevation is fixed, and the downstream-most 1.0 m of the flume consists of straight channel walls. We chose this outlet configuration to provide controlled conditions for water and sediment leaving the flume, which pass through the particle imaging light box for flux measurement (Fig. 5a, and discussed in more detail below). Figures 5a and 5b show that the experimental channel consists of downstream varying channel width, which for simplicity, reflects the interpolated width
10 condition between inflection points along a stream segment. We achieve the experimental width conditions by constructing a channel inside the flume with rough-faced veneer-grade D plywood, which has a surface roughness that varies from 1-4 mm, or roughly 0.15 to 0.60 times the geometric mean grain size of the experimental grain size mixture. The grain size distribution of the experiments ranges from 0.5–32 mm (Fig. 6), with a geometric mean size of 7.3 mm (D_g), a D_{90} of 21.3 mm, and a geometric standard deviation of 2.5 (σ_g). We used experimental water supply rates Q_w of 42, 60 and 80 liters per second
15 ($l\,s^{-1}$) with associated sediment supply rates of 0.5, 0.80 and 1.0 kilograms per minute ($kg\,min^{-1}$), respectively. Additional details about the experimental design are provided by Chartrand et al. (2018), and we note that the experimental grain size distribution and water supply rates are similar to those reported by (Kuhnle and Southard, 1988).

13
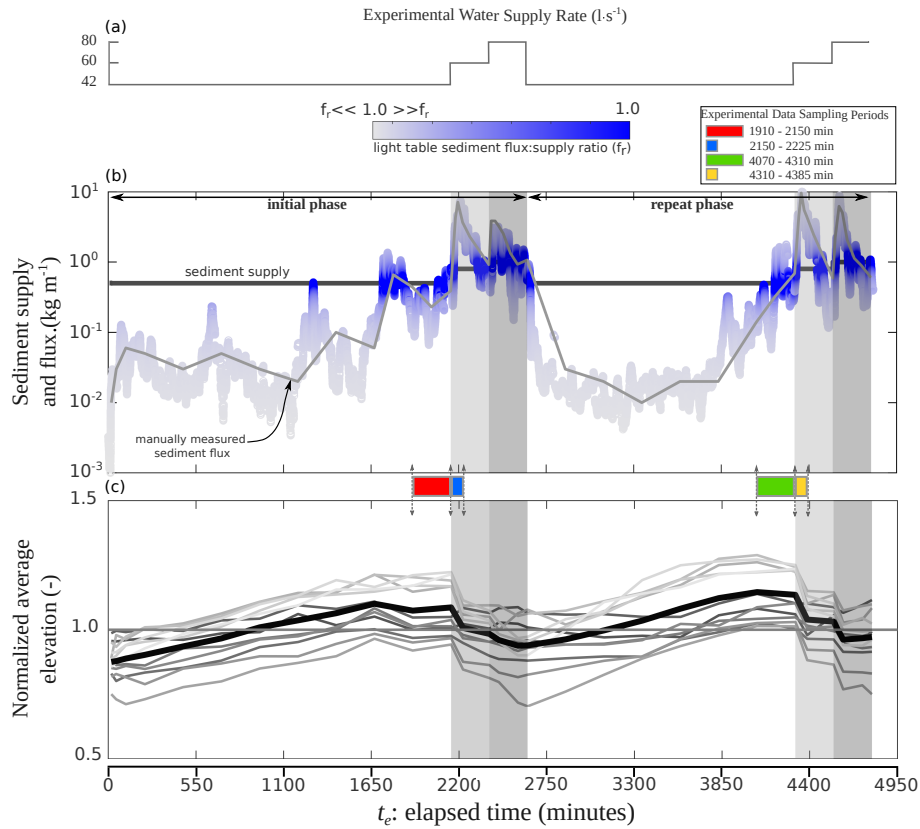
Figure 7. PRE1 details of water and sediment supply with evolution of bed elevation. (a) Timing and rate of flow during PRE1. (b) Timing and supply of sediment during PRE1. The first sequence of 42, 60 and 80 l s^{-1} water supply (and associated sediment feed) constitutes the initial experimental phase. The second flow and sediment feed sequence was the repeat phase. The vertical shaded areas reflect flow rates of 60 and 80 l s^{-1}, respectively, and the symbol color represents the ratio of sediment flux to sediment feed rate. (c) Temporal evolution of average bed elevation at the 12 subsampling locations shown in Fig. 5. The colored boxes indicate the time periods of PRE1 flux data analyzed herein.

3.1 Experimental procedure

We start PRE1 from a smoothed-bed, uniform slope condition. Prior to smoothing, the full thickness of sediment in the flume was mixed to establish a random size distribution, and to remove textural heterogeneity related to previous experiments. Figure 7a shows the experimental water supply rate in l s^{-1} versus time in minutes (a), the sediment supply rate in kg min^{-1} and

5 the 5-min moving average sediment flux in kg min^{-1} (b), and the average flume bed elevation (c). PRE1 had a total duration of 79.8 h, which consists of an initial and repeat phase (Fig. 7b). The initial phase extends from $t_e = 0$ min, where t_e is

Table 1. Details of the water and sediment supply rates

	Water Supply	Sediment Supply
	$\mathrm{l\,s^{-1}}$	$\mathrm{kg\,min^{-1}}$
Initial Phase		
0–2150 min	42	0.50
2150–2390 min	60	0.80
2390–2630 min	80	1.0
Repeat Phase		
2630–4310 min	42	0.50
4310–4550 min	60	0.80
4550-4790 min	80	1.0

1. L.T.: Light table total mass.

elapse time, to 2630 min, and the repeat phase extends from $t_e = 2630$ min, to 4790 min (Fig. 7b). Flow and sediment supply continue at constant values until the total sediment flux approximates the sediment supply rate, and in all cases the fractional flux was comparable to the fractional supply (Table 2; Fig. 7b). The specific water and sediment supply rates for PRE1 are provided in Table 1. We use a ramping up and down period of 4-5 min each time the water supply is raised and lowered to and from the experimental flows of 42, 60 and $80\,\mathrm{l\,s^{-1}}$. The repeat phase (Fig. 7b) began from the prevailing channel topographic and bed surface sediment sorting conditions established by the end of the initial phase (Fig. 7b).

3.2 Bedload flux

We use a light table to measure bedload flux and ensure mass conservation (Frey et al., 2003; Zimmermann et al., 2008). The light table system uses an overhead camera to measure particle positions in a water column 2 to 3 cm thick. The particles and water pass over a positively-sloping semi-transparent lexan base, which is backlit by a constant-voltage LED panel light measuring $610\,\mathrm{mm^2}$. Images of the silhouetted particles are captured at 15-20 Hz with an Allied Vision Technology GX2300 CCD camera. The camera uses a Kowa Optimed 16 mm 4/3" megapixel LM16XC lens, which was selected specifically for the GX2300 sensor resolution and imaging distance of the setup. Images are processed with LabView^{TM} code to compute the time-averaged flux for all grain size classes >2 mm at a temporal resolution of 1 Hz (Zimmermann et al., 2008). Here we report fractional flux results for grain size classes >4 mm in units of particles per second ($\mathrm{pa\,s^{-1}}$). The particle imaging setup went through extensive validation trials following Zimmermann et al. (2008). Throughout light table calibration and the experiment, all sediment passing through the light table was captured in a mesh catch basket. The catch basket was periodically emptied, sub-sampled, dried, sieved and compared to the light table data.

In the following subsection we describe analysis of the light table sediment flux time series for specified time durations of PRE1. The light table represents a fixed location in space, situated at the downstream end of the flume (Fig. 5). As a result, the flux time series reflects sediment transport conditions, and the associated particle number activity which occurs over a finite length at the downstream end of the flume (Eq. (4)). Approximating this length scale is difficult because it varies with

5 the macroscopic fluid conditions (e.g. Lajeunesse et al., 2010). However, we speculate a correlation between light table flux information and particle activity over 1–2 average channel widths of flume length, situated upstream of the flume exit.

3.3 Time Series Analysis

We examine time series of 1 Hz particle flux for four different time periods and six different grain size classes. The four different time periods consist of two sequences during which experimental conditions change from approximate statistical steady-state to

10 transient. We define approximate statistical steady-state (SS) by two different criteria. First, average bed elevation as recorded at 11 different locations along the experimental flume (Fig. 5) show a rate of change which tends to a constant, near zero value (Fig. 7c). Second, total sediment flux varies around the sediment supply rate (Fig. 7b) (cf. Dhont and Ancey, 2018). The change of overall experimental condition from steady-state to transient is due to an increase in the water and sediment supply rates from 42 to $60 \, \mathrm{l \, s^{-1}}$ and 0.5 to $0.8 \, \mathrm{kg \, min^{-1}}$, respectively (Figs. 7a and 7b). The two experimental sequences represent

15 the same upstream supply conditions, and only differ in terms of the initial bed profile and sediment texture conditions. As a result, the two sequences reflect generally paired and replicate conditions. The corresponding steady-state flux time series for the initial and repeat experimental phases are from elapsed times 1910–2150 (herein referred to as t1910) and 4070–4310 min (herein referred to as t4070), respectively (Fig. 7b). The corresponding transient flux time series for the initial and repeat experimental phases are from elapsed times 2150–2225 (herein referred to as t2150) and 4310–4385 min (herein referred to as

20 t4310), respectively (Fig. 7b).

We use several different methods to learn about and characterize the flux time series. We plot the fractional flux as histograms, calculate Poisson and negative binomial probability mass function (pmf) fits, and calculate descriptive statistics. The Poisson and negative binomial distributions represent steady-state conditions for the particle number activity γ of a streambed area A as $t \to \infty$, depending on whether $\mu = 0$, or $\mu > 0$, respectively (Ancey et al., 2008). Recall our assumption that the particle

25 number activity γ measured within the streambed area A upstream from the light table is directly proportional to γ^* measured on the light table (Eq. 4). Consequently, we expect the probability mass distribution of γ^* measured on the light table to approximate a Poisson or negative binomial, again depending on whether $\mu = 0$, or $\mu > 0$, respectively. As a result, we use the PRE1 flux to directly test Ancey and colleagues steady-state solution for their birth-death Markov process model, which we expand here for sediment mixtures. We note, however, that the PRE1 flux data used for this test represents both steady-state

30 and transient experimental conditions (Fig. 7). For the transient conditions, we assume that the relatively large sample size N for each grain size class (see Table 3) justifies approximating the binomial distribution of the general birth-death model solution (Ancey et al., 2008) as a Poisson distribution, and as a negative binomial distribution depending on contributions from collective entrainment. We calculate Poison distribution fits using the optimize and curve fit tool boxes of the SciPy Python Library (Jones et al., 2001). Bin middle values and associated histogram results for the experimental flux time series are inputs

16

for the distribution parameters k and λ, respectively. We calculate negative binomial distribution fits using the methods of moments introduced by Pafnuty Chebyshev in 1887 (Goswami et al., 2019). Notably, we calculate p as $E[X]/V[X]$ in order to be consistent with Ancey et al. (2008), who represent p as the probability of observing any particular value γ within a control volume above some bed area A, and at any instant in time. See Chartrand et al. (2020) for the source codes within which the calculations are made.

We apply discrete Fourier transform to the fractional flux time series to examine the distribution of spectral density across frequencies from 10^{-3} to $10^{-0.5}$ Hz. Each fractional flux time series was preprocessed according to several steps before calculating the power spectral density. Preprocessing began by removing anomalous signals related to memory caching problems. Anomalous signals are identified with an internal error code related to the circumstance of insufficient image information during calculation of the 1 Hz average flux values for each grain size class. Anomalous signals have 1 Hz average flux values that are 2–3 orders of magnitude higher than nearby rates, and generally persist for 1 to 2 s. A total of 2.47% of the raw flux data for t1910, were anomalous, 1.60% for t4070, 0.89% for t2150 and 0.42% for t4310. After removal, the anomalous values were replaced by the mode of the preceding 20 s time interval, or shorter if the anomalous values occurred at the beginning of a data collection period. We selected 20 s for mode calculation because the longest string of anomalous values was 19 s. All signal processing discussed next was completed using the signal toolbox of the SciPy Python library (Jones et al., 2001).

A Tukey window with a shape factor 0.5 was first applied to the raw fractional flux time series. Windowing results in a smoothed beginning and end of the respective time series, which lessens spectral leakage and edge effects related to the time series finite length and signal amplitude at the time series edges. A Tukey window with shape factor 0 is equivalent to a rectangular window and a shape factor of 1 is equivalent to a Hann window. The power spectral density of the windowed fractional flux time series was then calculated with the fast Fourier transform (FFT) Welch's method using a Hann window, equal to the square of the real $\Re$ components of the resultant Fourier coefficients. The input Tukey windowed data are detrended by removing the mean of each time series, and then the FFT is calculated for overlapping data segments of length $N_{ps} =$ 1,028 values. This means the windowed time series are sliced into data segments that are N_{ps} points long, and overlap by $N_o = N_{ps}/2$ data points. The resulting modified periodograms for each data segment are then averaged to return the estimated power spectral density for each Tukey windowed, grain size class time series. Welch's method of calculating the power spectral density reduces low frequency content through slicing and averaging at the expense of power spectral density resolution. For comparison, we also computed the FFT for each grain size class and time series using Tukey window shape factors of 0.25 and 0.75, and observed no meaningful difference in the results. Last, we calculate the autocorrelation of the four sediment flux time series, for each of the six different grain size classes using the windowed and detrended data.

3.4 Sources of Uncertainty

The light table has uncertainty related to the ability to resolve grain diameter within the backlit photographic frame. This challenge arises from a variety of sources, including the camera/lens resolution, spatial consistency of the light table output lumens and particle edge resolution (see Zimmermann et al., 2008, for other considerations). As a result and based on pre-experiment calibration tests, we do not report flux results for grain sizes < 4 mm.

Table 2. Details of the light table results

	Steady-state		Transient	
	t1910	t4070	t2150	t4310
$^{L.T.}/_{C.B.}$	1.01	1.07	0.91	0.92
4 mm	$^{0.13}/_{0.12}$	$^{0.10}/_{0.08}$	$^{0.12}/_{0.12}$	$^{0.12}/_{0.12}$
5.6 mm	$^{0.15}/_{0.17}$	$^{0.15}/_{0.14}$	$^{0.14}/_{0.15}$	$^{0.15}/_{0.15}$
8 mm	$^{0.17}/_{0.17}$	$^{0.20}/_{0.18}$	$^{0.16}/_{0.16}$	$^{0.17}/_{0.16}$
11.3 m	$^{0.24}/_{0.28}$	$^{0.24}/_{0.28}$	$^{0.19}/_{0.20}$	$^{0.19}/_{0.22}$
16 mm	$^{0.13}/_{0.15}$	$^{0.15}/_{0.19}$	$^{0.11}/_{0.13}$	$^{0.11}/_{0.13}$
22.6 mm	$^{0.04}/_{0.04}$	$^{0.07}/_{0.09}$	$^{0.05}/_{0.05}$	$^{0.06}/_{0.07}$

1. L.T.: Light table total mass.

2. C.B.: Catch basket total mass.

3. The ratios $^{n}/_{d}$ for each grain size class indicates light
   table fractional mass to sieve sample fractional mass.

The light table images were processed by setting threshold gray scale values to isolate sediment particles against the backlit lexan sheet. For any one experimental interval, one or more image processing runs were needed to achieve as close a match as practical to the total mass measured by the sediment catch-basket. An exact match between light table total mass and catch basket total mass is impossible. For example, the light table mass for each grain size fraction is calculated by multiplying the
5   1 Hz grains-size specific particle activity by the average mass for each grain size class (Chartrand et al., 2018).

Despite these challenges, the light table results show good agreement with the basket captured total and fractional masses (Table 2). The top row of Table 2 shows that the ratio between light table total mass and catch basket total mass ranged from 0.91–1.07. Rows 2–7 show the ratios of the fractional masses between light table and a sieved sample from the catch basket total mass. Absolute differences between the fractional masses ranges from 0–0.04. These basic descriptions set the limit of
10 our ability to characterize measurement uncertainty of the light table. This is primarily because we use different gray scale threshold values between measurement time intervals when processing the light table images. Threshold values differences were necessary due to changes in the ambient lighting condition of the laboratory.

Table 3. Descriptive statistics for the 1 Hz bedload flux time series

|		Steady-state		Transient	
		t1910	t4070	t2150	t4310
	TTSD (sec.)	14,396	14,245	4,582	4,529
	4 mm	21,168	27,620	79,965	97,674
	5.6 mm	11,127	17,767	38,741	47,230
	8 mm	5,101	9,180	17,641	21,668
Total Particle Count	11.3 m	3,200	5,5591	9,612	11,620
	16 mm	918	1,670	2,687	3,081
	22.6 mm	87	274	410	568
	Total	**41,601**	**62,102**	**149,056**	**181,841**
	4 mm	0	0	0	0
	5.6 mm	0	0	0	0
Minimum Particle Count	8 mm	0	0	0	0
	11.3 mm	0	0	0	0
	16 mm	0	0	0	0
	22.6 mm	0	0	0	0
	4 mm	22	36	112	121
	5.6 mm	10	20	45	54
Maximum Particle Count	8 mm	6	11	19	26
	11.3 mm	5	9	12	15
	16 mm	3	7	6	6
	22.6 mm	3	3	4	4
	4 mm	0	0	5	2
	5.6 mm	0	0	5	4
Mode of Particle Count	8 mm	0	0	2	2
	11.3 mm	0	0	0	1
	16 mm	0	0	0	0
	22.6 mm	0	0	0	0
	4 mm	1	0	13	17
	5.6 mm	0	1	7	9
Median of Particle Count	8 mm	0	0	3	4
	11.3 mm	0	0	2	2
	16 mm	0	0	0	0
	22.6 mm	0	0	0	0
	4 mm	4	5	37	48
	5.6 mm	2	4	17	22
90th Percentile of Particle Count	8 mm	1	2	8	10
	11.3 mm	1	1	5	6
	16 mm	0	0	2	2
	22.6 mm	0	0	0	1
	4 mm	1.47	1.94	17.42	21.57
	5.6 mm	0.77	1.25	8.44	10.43
Mean of Particle Count	8 mm	0.35	0.64	3.84	4.78
	11.3 mm	0.22	0.39	2.09	2.57
	16 mm	0.06	0.12	0.59	0.68
	22.6 mm	0.01	0.02	0.09	0.13
	4 mm	3.39	10.2	203.2	332.4
	5.6 mm	1.24	3.93	41.1	66.7
Variance of Particle Count	8 mm	0.50	1.25	9.19	14.1
	11.3 mm	0.30	0.65	3.56	4.91
	16 mm	0.08	0.16	0.73	0.90
	22.6 mm	0.01	0.03	0.10	0.16

1. TTSD: Total Time Series Duration
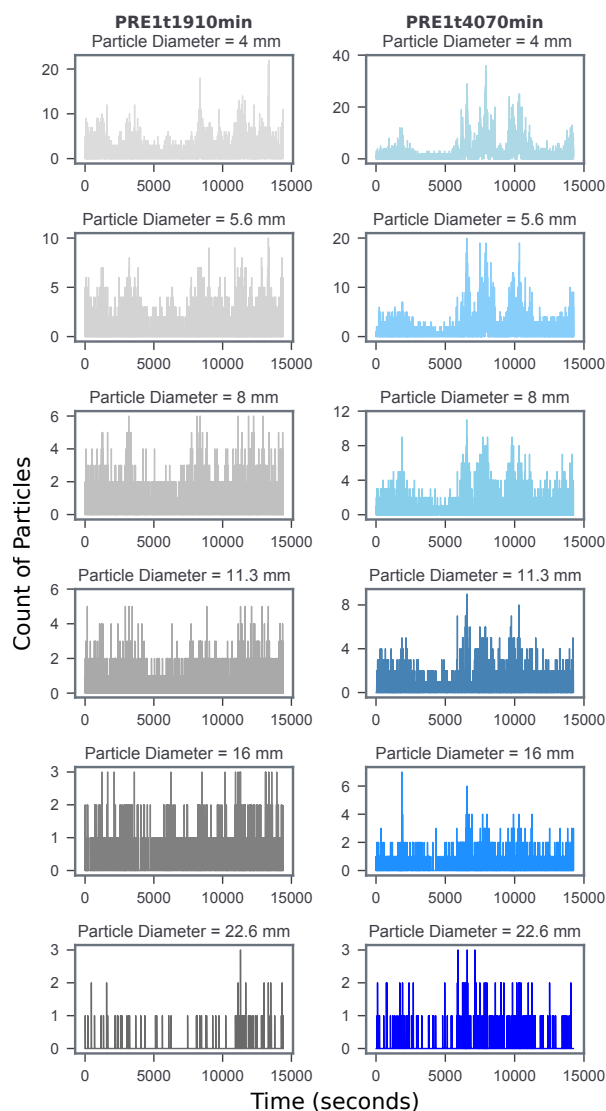
Figure 8. Time series of 1 Hz fractional sediment flux for experimental elapsed times 1910–2150 and 4070–4310 min. These two time periods correspond to approximate statistical steady-state conditions, and for the same upstream supply of water and sediment. Fractional sediment flux reported reported for the retaining sieve size.

4 Results

4.1 Approximate Steady-State Flux

Statistical steady-state flux is characterized by a time-varying signal across all grain size classes, and ranges from approximately 0–40 pa s^{-1} (Table 3; Fig. 8). Flux magnitude and signal continuity are correlated with grain size (Fig. 8). Finer grain size
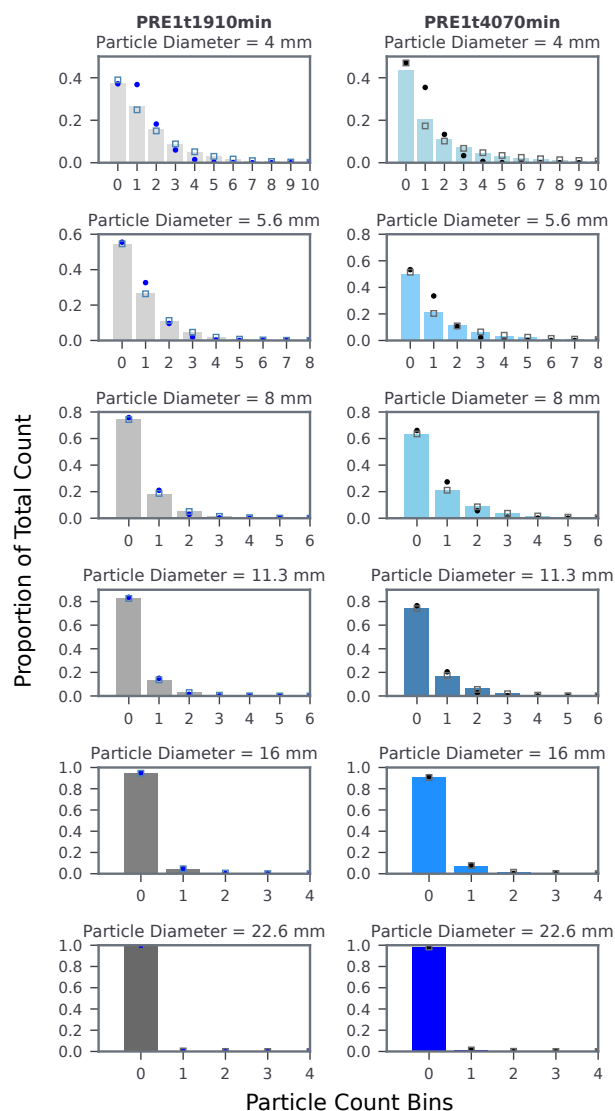
Figure 9. Histograms of 1 Hz fractional sediment flux for experimental elapsed time 1910–2150 and 4070–4310 min. The filled circles are Poisson probability mass function fits to the fractional flux data, and open squares are negative binomial fits.

fractions from 4–11.3 mm have particle counts that range from approximately 0–40 pa s^{-1} (Table 3), and are discontinuous in time. The time discontinuity of the 1 Hz flux increases with particle size.

Flux modes for the finer grain size fractions is zero, and the median is nonzero in only two instances across both time series. The mean flux, on the other hand, is nonzero for all finer size classes, and the variance extends over a wide range of values 5 (Table 3). However, the mean flux magnitude for the finer size classes is sensitive to the aggregation time interval (Fig. A1).

For example, the t4070 mean flux of the 4 mm particle size varies by up to a factor 4 for aggregation time intervals that range from $t/20$–t, where t is the total time duration of the measurement interval. For t4070 $t = 240$ min.

Flux magnitude for coarser grain size fractions from 16 to 32 mm, on the other hand, have a range from approximately 0–10 pa s^{-1}, and have a greater proportion of periods of zero flux (Table 3; Figs. 8 and 9). This last point is most clear in the

5 record for the coarsest grain size fraction (22.6–32 mm), which has periods of zero flux that range from 10 to 100 s or more in duration (Fig. 8). The mode and median of the coarser grain size fractions is 0 (Table 3). However, the mean is nonzero in all cases. The positive skew of the steady-state fractional fluxes decreases with grain size (Fig. 9).

Maximum flux for the finer grain size fractions are associated with short durations of elevated transport that are embedded within an increasing background flux (Fig. 8). During the sharp rises in transport, particle counts increase by a factor 2–3

10 above the preceding particle counts, and persist at these elevated conditions for seconds to minutes (Fig. 8). This is the case for coarser grain size fractions as well, but the magnitude of the sharp flux increases is smaller than that for finer size fractions by a factor of 2 to 3.

Probability mass function fits to the flux histograms is grain size dependent (Fig. 9). The 4–8 mm grain size classes show better overall agreement with the negative binomial pmf, whereas the 11.3–22.6 mm size classes are in general fit equally well

15 by the Poisson pmf and negative binomial pmf.

4.2 Transient Flux

Transient flux is elevated compared to statistical steady conditions and is characterized by a time-varying signal across all grain size classes that ranges from approximately 0–120 pa s^{-1} (Table 3; Fig. 10). Flux magnitude and signal continuity is correlated with grain size (Fig. 10). Finer grain size fractions from 4–11.3 mm have particle counts that range from approximately 0–120

20 pa s^{-1} (Table 3), and flux is discontinuous in time, but less so than the steady-state case. Signal discontinuity increases with grain size.

The flux modes for the finer grain size fractions ranges from 0–5, and the median ranges from 2–17 (Table 3). The mean flux is nonzero for all finer size classes, and the variance extends over a wide range of values (Table 3). However, the mean flux magnitude for the finer size classes is sensitive to the aggregation time interval (Fig. A1). For example, the t4310 mean flux of

25 the 4 mm particle size varies by up to a factor 1.7 for aggregation time intervals that range from $t/20$–t. For t4310 $t = 75$ min.

Flux magnitude for coarser grain size fractions from 16 to 32 mm, on the other hand, have a range from approximately 0–10 pa s^{-1}, and have a greater proportion of periods of zero flux (Table 3; Figs. 10 and 11). This last point is most clear in the record for the coarsest grain size fraction (22.6–32 mm), which has periods of zero flux that range from 1 to 10 s or more in duration. The mode and median of the coarser grain size fractions is 0 (Table 3). The mean flux, however, is nonzero for the

30 coarser size classes. The variance is comparable to the mean (Table 3). Similar to the steady-state results, the positive skew of the transient fractional fluxes decreases with grain size (Fig. 11).

Similar to the steady-sate case, maximum flux for the finer grain size fractions are associated with short durations of elevated transport that are embedded within an increasing background rate of transport (Fig. 10). During the sharp rises in transport, particle counts increase by a factor 2–3 above the immediately preceding particle counts, and persist at these elevated conditions
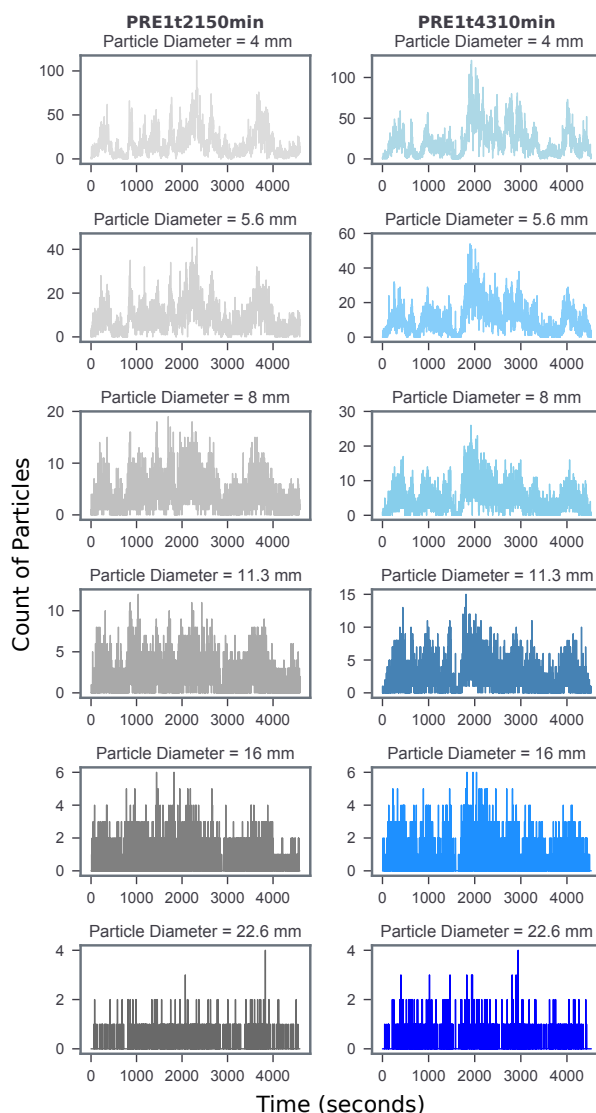
Figure 10. Time series of 1 Hz fractional sediment flux for experimental elapsed time 2150–2225 and 4310-4385 min. These two time periods correspond to approximate statistical steady-state conditions, and for the same upstream supply of water and sediment. Fractional sediment flux reported reported for the retaining sieve size.

for seconds to minutes (Figs. 10). This is the case for coarser grain size fractions as well, but the magnitude of the sharp flux increases is lower than that for finer size fractions by factors of 2 to 20.

Probability mass function fits to the flux histograms is grain size dependent, and more strongly so compared to the steady-state case (Fig. 11). The 4–8 mm grain size classes show remarkable agreement with the negative binomial pmf, and the fit
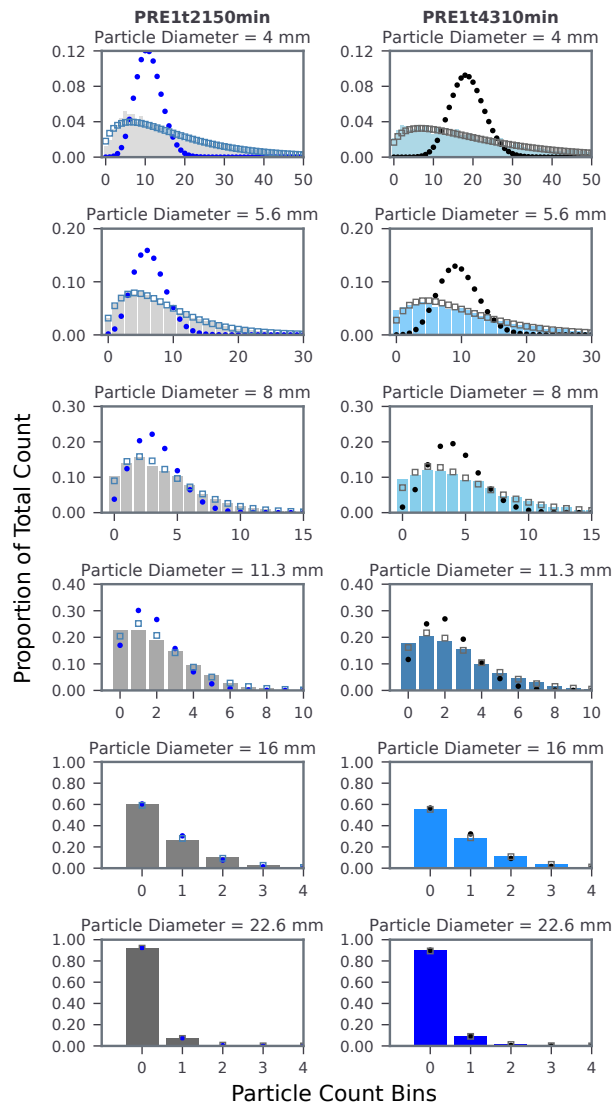
Figure 11. Histograms of 1 Hz fractional sediment flux for experimental elapsed time 2150–2225 and 4310–4385 min. The filled circles are Poisson probability mass function fits to the fractional flux data, and open squares are negative binomial fits.

with the 11.3 mm size class is also good. The coarsest two grain sizes, on the other hand, are in general fit equally well by the Poisson pmf and negative binomial pmf.

4.3 Approximate steady-state power spectral density

Figure 12 shows that the normalized power spectral density (*NPSD*) estimates for approximate steady-state conditions differs
5   according to grain size class. The spectra are normalized by the maximum spectral density of the 4 mm grain size class in order
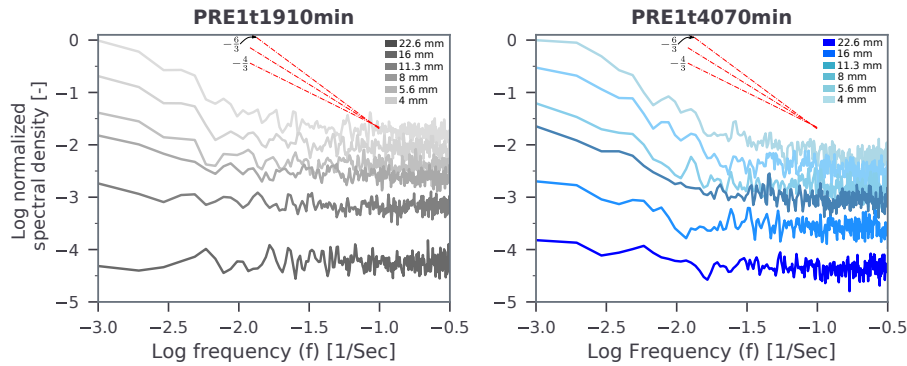
Figure 12. Estimated power spectral density by grain size class for the steady-state time series of sediment flux, normalized by the maximum power of the 4 mm grain size class. The dashed red lines provide reference lines of different slope.

to examine how the specific grain size spectra compare to the power of the smallest size class. The smallest grain size class 4 mm has the largest magnitude *NPSD*, and the largest grain size class 22.6 mm has the smallest magnitude *NPSD*. In between these two bounding grain size classes, the *NPSD* decreases as grain size increases. Relative to the maximum power of 4 mm, the *NPSD* span roughly 5 orders of magnitude.

5   The distribution of spectral density across the range of frequencies also differs according to grain size class. The *NPSD* for grain size classes 4–11.3 mm have corner frequencies f_c of approximately $10^{-2.5}$ Hz. The *NPSD* decreases proportionally as $1/f^{-\frac{6}{3}}$ to $1/f^{-\frac{4}{3}}$ for frequencies in the approximate range 10^{-3} to $10^{-1.8}$. In contrast, the *NPSD* for grain size class 16 mm decreases proportionally as $1/f^{-1}$ to $1/f^{-\frac{1}{3}}$, and the *NPSD* for the 22.6 mm size class is distributed with roughly equal spectral density across all frequencies.

10   The approximate steady-state distribution of spectral density for the grain sizes evaluated here changes if the input data are represented differently. For example, Fig. B1 shows the *NPSD* calculated using 1 Hz particle mass estimates. The mass-based normalized spectral density magnitude is size dependent, similar to the particle count based *NPSD* results (Fig. 12). However, the larger grain size classes account for a greater proportion of the total and maximum spectral density, compared to the smaller size classes, because particle mass is proportional to the diameter cubed.

15   **4.4   Transient power spectral density**

Similar to the steady-state results, the transient *NPSD* estimates differ according to grain size class (Fig. 13). The smallest grain size class 4 mm has the largest magnitude *NPSD*, and the largest grain size class 22.6 mm has the smallest magnitude *NPSD*. In between these two bounding grain size classes, the *NPSD* decreases as grain size increases. Relative to the maximum power of 4 mm, the *NPSD* span roughly 5 orders of magnitude.

20   The distribution of spectral density across the range of frequencies also differs by grain size class. The *NPSD* for grain size classes 4–16 mm have corner frequencies f_c of approximately $10^{-2.5}$ Hz. The *NPSD* decreases proportionally as $1/f^{-\frac{6}{3}}$ to $1/f^{-\frac{4}{3}}$ for frequencies in the approximate range 10^{-3} to $10^{-1.8}$. In contrast, the *NPSD* for grain size class 22.6 mm

25
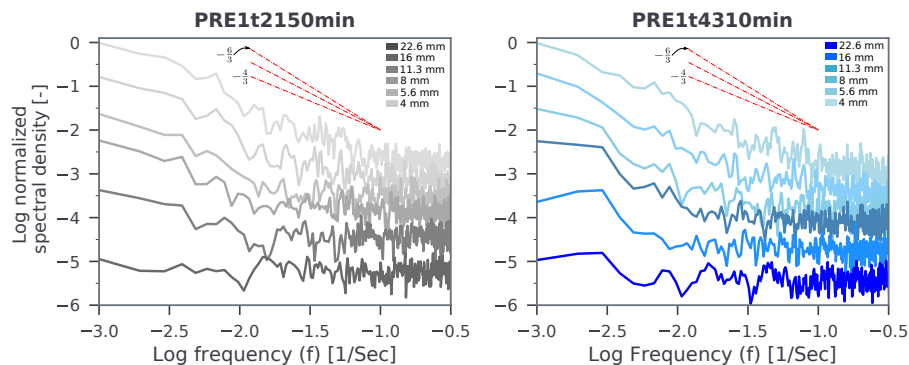
Figure 13. Estimated power spectral density by grain size class for the transient time series of sediment flux, normalized by the maximum power of the 4 mm grain size class. The dashed red lines provide reference lines of different slope.

is distributed with roughly equal power across all frequencies. Last, the distribution of transient spectral density changes if particle counts are represented by estimated equivalent masses (Fig. B2). Similar to the steady-state case, the mass-based size dependent distribution of *NPSD* for transient conditions shows that the larger grain size classes account for a greater proportion of the total and maximum spectral density, compared to the smaller size classes.

4.5 Approximate steady-state and transient autocorrelation

Autocorrelation of sediment flux varies with grain size class for steady-state and transient conditions (Figs. 14 and 15). Smaller grain sizes show stronger autocorrelation with roughly exponential behavior through lags of $\approx$250–500 s. Autocorrelation strength and time decreases with grain size, and in general, flux of the largest two grain size classes is uncorrelated in time, and exhibits a white noise type structure. Comparison of the two sets of results reveals that the transient autocorrelation is stronger than the steady-state case for the 4–11.3 mm grain size classes (Figs. 14 and 15).

5 Discussion

5.1 Transport behaviour of gravel-rich sediment mixtures

Flux measurements for PRE1 made with a light table device indicate bedload transport is characterized by a fluctuating time signal, regardless of grain size (e.g. Iseya and Ikeda, 1987; Kuhnle and Southard, 1988; Frey et al., 2003; Saletti et al., 2015). However, the grain size specific fluctuations represent different transport behaviours. Grain sizes between 4 and 16 mm exhibit stronger time correlated transport behaviour, whereas grain sizes between 16 and 32 mm exhibit increasingly weaker behaviour (Figs. 8–15). The contrasting transport behaviour for small versus large grains describes both steady-state and transient bed topography conditions (Fig. 7c) (see Chartrand et al., 2018, 2019). Physically, a congruence of particle flux behaviours between differing rates of bed topography adjustment and bedload transport stages suggests a common set of physical mechanisms are

26

responsible for bedload transport. Saletti et al. (2015) report similar results, and find that smaller particle sizes tended to exhibit time correlated transport behaviour, whereas increasingly larger grain sizes tended to time uncorrelated behaviour (also see Kuhnle and Southard, 1988).

Consistency between our results and the work of Saletti et al. (2015), and to some extent Kuhnle and Southard (1988),
5 is notable because the experimental conditions differed. The bedload transport data summarized here reflects experiments conducted to examine the development of pool-riffle channel segments within a variable width flume (cf. Chartrand et al., 2018, 2019). In contrast, Saletti et al. (2015) report on bedload transport measured during the experimental development of step-pool channel segments, and Kuhnle and Southard (1988) report experiments conducted within uniform width flumes designed to examine bedload transport behaviour. The PRE1 experiments were conducted with steady supplies of sediment
10 at three different water supply rates. Kuhnle and Southard (1988) also used steady upstream supplies of sediment and water, however their sediment supply rates were up to an order of magnitude greater than rates for PRE1. Saletti et al. (2015), on the other hand, report results of experiments for which the water and sediment supply were varied in a more complicated manner. Despite these differences of experimental design, a consistent size dependent transport behaviour for sediment mixtures is evident. This finding raise an important question: what physical mechanisms might contribute to similar grain size dependent
15 transport behaviour across differing bed architectures, channel slopes and driving conditions? The exploratory three particle size birth-death model generally supported by our experimental results suggests that fluid and collective entrainment, and the interplay between these mechanisms, offers one possible explanation (e.g. Eqs. 15–17) (Figs. 3–4, 9 and 11). We elaborate this proposal below by discussing our visual observations of how bedload transport occurred within the flume during PRE1.

We observed several different transport processes during PRE1 that are consistent with previous work, and which together
20 provide context for the birth-death model presented in Section 2. During the steady-state periods t1910 and t4070, particles commonly moved along roughly straight, downstream-oriented transport pathways, including up and to the flume outlet. These pathways were located within the central part of the flume, and the pathways commonly extended for distances of several meters in length (e.g. Powell, 1998; Dhont and Ancey, 2018). The specific location of the pathways might have been controlled by local topographic conditions (e.g. Powell, 1998), but we are not able to demonstrate this effect. Particle sizes up to approximately
25 16 mm moved within these zones, which often exhibited a consistent transport of grains. As the transport intensity increased during the transient conditions t2150 and t4310, the number of transport pathways increased, and some merged (cf. Lee and Jerolmack, 2018). However, in both cases, it was uncommon to observe more than the occasional grain from the coarsest size classes moving within the pathways. By comparison, the coarsest grains tended to move along pathways that were related to the particles original position relative to the flume walls. We interpret the near time-continuous transport of grains along
30 preferential pathways as a key contribution to the average particle flux for grain sizes up to approximately 16 mm, which is sensitive to the averaging time scale (Figs. A1 and A2) (Kuhnle and Southard, 1988; Bunte et al., 2004; Singh et al., 2009; Saletti et al., 2015; Dhont and Ancey, 2018; Ancey and Pascal, 2020).

We also observed gravel-dune type features many D_{50} grain diameters tall (Carling, 1999; Chartrand et al., 2017, 2018, see Fig. 7, t2150 of the latter), and to a lesser degree bedload sheets a few D_{50} grain diameters tall (Whiting et al., 1988; Kuhnle
35 and Southard, 1988; Dhont and Ancey, 2018, e.g.). We did not observe the systematic longitudinal grain sorting reported

by Iseya and Ikeda (1987), but the experimental beds were commonly congested in appearance. Both bedload features were observed during steady-state and transient periods, however it was easier to observe the gravel dunes move to the flume outlet intermittently, and result in elevated particle flux that lasted for durations of up to minutes. Unlike the gravel bars reported by Dhont and Ancey (2018), neither gravel-rich feature observed here were consistent attributes of the bed architecture along the

5 flume, which suggests other transport mechanisms such as collective entrainment contributed to the fractional flux measured by the light table (Figs. 8 and 10). We note, though, that the duration of our experiments was short compared to those reported by Dhont and Ancey (2018), and as a result our interpretation of flux-related affects for gravel-dune type features and bedload sheets may be biased.

Based on limitations of our experimental measurements, we cannot assign a specific entrainment mechanism to the down-
10 stream motion of sediment particles (Singh et al., 2009). However, the combination of fluid and collective entrainment, and the grain size dependent interplay between these mechanisms provides a plausible explanation. General consistency between the theoretical predictions of the Ancey and colleagues birth-death model (Ancey et al., 2008; Ancey, 2010, and also see Heyman et al. (2013) and Heyman (2014)), illustrated behaviour of the exploratory three particle size birth-death model developed here (Figs. 3–4), and our experimental results support this perspective. In particular, negative binomial distribution fits to flux his-
15 tograms for smaller particles size classes of PRE1 is consistent with birth-death formulation involving collective entrainment (Figs. 9 and 11). Going forward, substantial work remains to more explicitly connect mechanisms of entrainment, etc. within gravel-bed river segments to bedload transport processes and associated measurements. To this end, in the next section we discuss testable links between transport fluctuations and the physics of bedload transport, and in our concluding remarks we suggest one path forward to examine identified links.

20 ## 5.2   What controls the power spectral density of the particle flux?

We hypothesize that the power spectra of bedload transport within gravel-bed rivers at low to moderate transport stages (Hassan et al., 2005) can be conceptually explained by covariations and interplay between the rates of fluid-driven and collective entrainment of particles, as well as rates of particle deposition (Figs. 3–4) (see video supplement–Chartrand (2017)). At time scales much larger than bedload particle travel times of fractions or a few seconds or more (cf. Drake et al., 1988; Roseberry
25 et al., 2012; Fathel et al., 2015), we envision that fluid-driven particle entrainment of any grain size fraction λ_j sets a baseline local activity, which can preferentially amplify the lower frequency content for smaller grain size classes (Figs. 3, 4, 12 and 13). The baseline flux is represented by a combination of a Poisson process for the transport behaviour of larger grain size classes, whereas smaller size classes exhibit a more time-persistent transport behaviour, with increasing correlation or memory at short time scales (Figs. 14 and 15) (Saletti et al., 2015).
30 Collective entrainment can further amplify the baseline activity across all overlapping frequencies, with a clear emphasis on lower frequencies (Figs. 3 and 4). An emphasis on lower frequencies is related to the low-pass behaviour of Eqs. (8 and 15–17). The amplifying effect of collective entrainment in setting the magnitude of the power spectra is maximized as $\mu_j \rightarrow \sigma_j$. Conversely, the collective entrainment effect diminishes for $\sigma_j >> \mu_j$. Although we cannot definitely demonstrate that collective entrainment contributed to the grain size specific power spectra for PRE1 (Figs. 12 and 13)), two additional pieces of
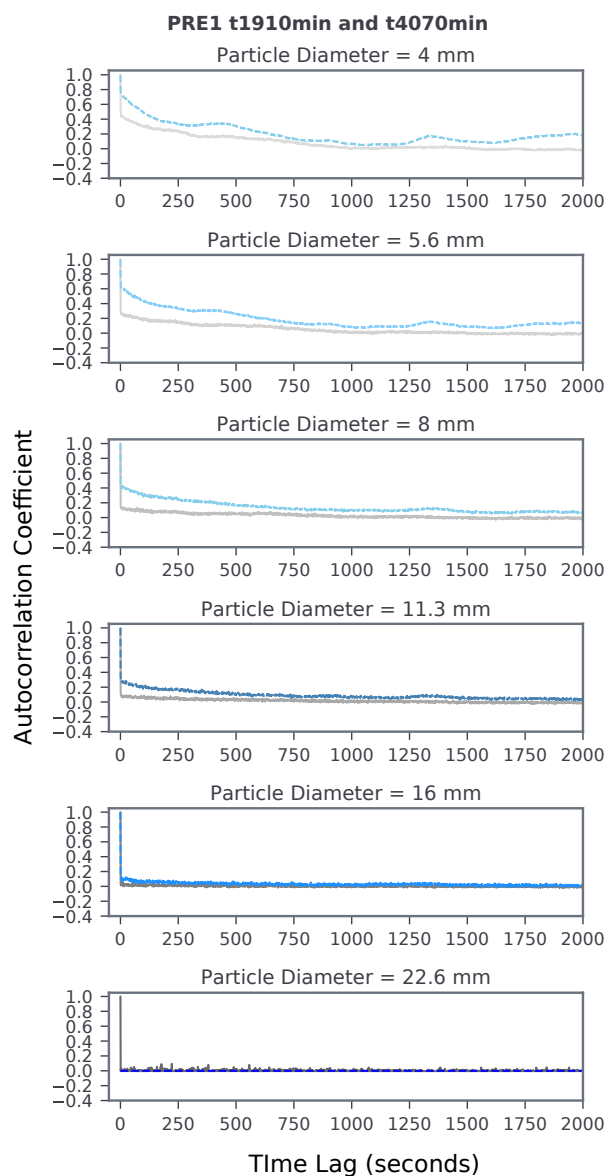
Figure 14. Autocorrelation of windowed and detrended sediment particle flux time series for t1910 (gray curves, solid lines) and t4070 (blue curves, dashed lines). The autocorrelation has been truncated at a time lag of 2,000 s.

evidence support this interpretation. First, the PRE1 power spectra structure is generally consistent with that for our exploratory 3–particle birth-death system. Consistency occurs when the collective entrainment rate across all particles sizes is relatively large, and/or the autoregressive temporal correlation for smaller particle sizes is large relative to coarser particles (Fig. 4). Second, and as mentioned above, histograms of particle flux for smaller particles sizes of PRE1 show agreement with the

negative binomial distribution pmf (Figs. 9 and 11). This outcome supports the theoretical prediction of Ancey et al. (2008) for conditions when $\mu > 0$, and the combination of evidence suggests an important role for collective entrainment to the transport of gravel mixtures (Fig. 3) (e.g. Ancey et al., 2006, 2008; Singh et al., 2009; Ancey, 2010; Heyman et al., 2013; Heyman, 2014; Masteller and Finnegan, 2017; Lee and Jerolmack, 2018). As a result, our work adds to the growing recognition for the need

5   for an expanded model of bedload transport (e.g. Ancey, 2010; Furbish et al., 2012a; Lee and Jerolmack, 2018; Yager et al., 2018b).

The local mixing of fluid and collective entrainment signals, less the effect of deposition, involves the physical coincidence of differing distributions of particle travel lengths and durations, and with particles at different points along a travel pathway (e.g. Fig. 3). In particular, we hypothesize that it is the interplay between these different phenomena combined which yields

10   power spectra that fall off with increasing frequency for finer grain sizes, and which reduces to a white noise for grain sizes that approach the mixture limiting size (Figs. 3, 4, 12 and 13). These results are not unique, and appear to represent a basic attribute of granular transport systems. For example, experimental results reported by Jerolmack and Paola (2010) and Dhont and Ancey (2018) show total transport power spectra which fall off at slopes between $1/f^{-\frac{3.5}{3}}$–$1/f^{-\frac{4.5}{3}}$ for increasing frequency, respectively. In Fig. C1 we provide composite spectral density distributions for PRE1, and find that fall off slopes for both steady-state

15   and transient conditions range from $1/f^{-\frac{5}{3}}$–$1/f^{-\frac{4}{3}}$ for the frequency range 10^{-3}–$10^{-0.5}$. The frequency range reported by Dhont and Ancey (2018) is notably lower than that reported here. Nonetheless, overall consistency between the three data sets in terms of the power spectra structure implies that similar bedload transport processes are responsible. Consequently, our work re-emphasizes the need to better understand controls on differences in how relatively small versus large grains are transported in rivers, because the mechanics of sediment mixture transport is not deterministic at any rate of motion (e.g. Einstein, 1937,

20   1950; Jackson and Beschta, 1982; Hassan et al., 1991; Ancey, 2010; Lajeunesse et al., 2010; Furbish et al., 2012a, b; Heyman et al., 2013; Fathel et al., 2015; Saletti et al., 2015; Furbish et al., 2017; Masteller and Finnegan, 2017; Lee and Jerolmack, 2018; Yager et al., 2018a).

6   Concluding Remarks and Next Steps

Four time series of particle flux for steady-state and transient bed elevation reveals both consistent and contrasting transport

25   behaviours across six different grain sizes. First, particle transport as bedload is characterized by a fluctuating time signal, regardless of grain size. Second, the fluctuating signals encode transport behaviour differences that depend on grain size. Notably, the motions of finer grain sizes are strongly correlated in time, whereas the transport of coarser grain sizes is weakly correlated in time. These results are supported by descriptive statistics, power spectral analysis and autocorrelation results, and are consistent with the results of Saletti et al. (2015).

30   An expanded Markov birth-death model (Ancey et al., 2008; Ancey, 2010; Heyman, 2014) offers a plausible explanation for grain size dependent transport behaviour of gravel mixtures. The interplay between fluid-driven and collective entrainment, less the effect of deposition, locally amplifies the activity of increasingly smaller grain sizes. This affect is propagated downstream through the full distribution of particle motions, and the result is to increase the amplitude of the lower frequency component
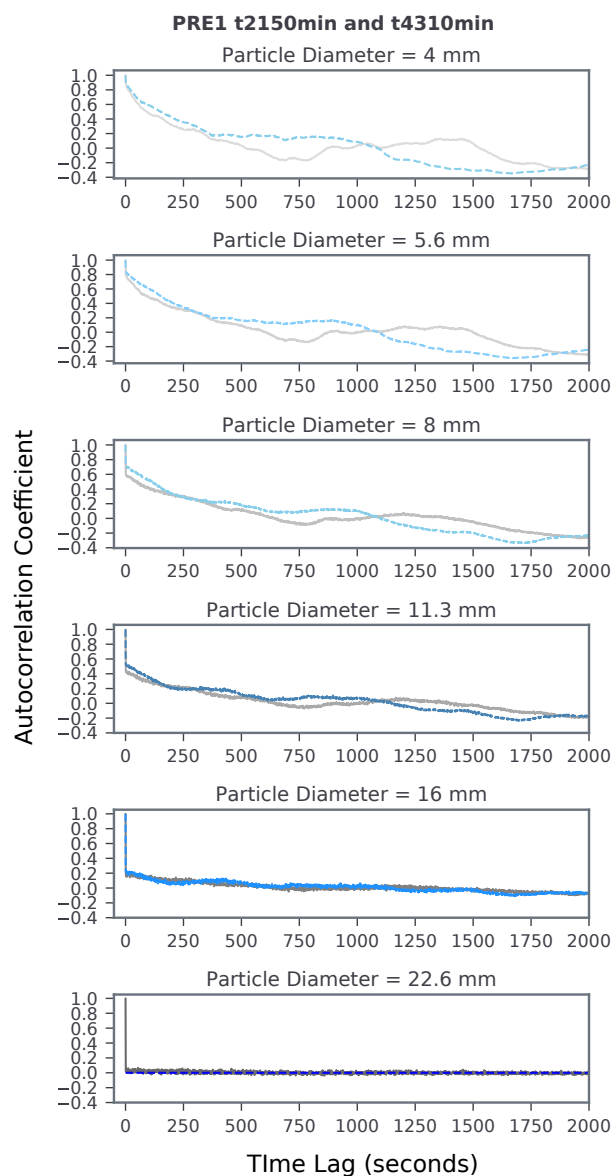
Figure 15. Autocorrelation of windowed and detrended sediment particle flux time series for t2150 (gray curves, solid lines) and t4310 (blue curves, dashed lines).

of flux signals, with an emphasis on smaller grain sizes. Grain size dependent negative binomial fits to flux histograms further supports our interpretation, as well as the theoretical result of Ancey et al. (2008), and suggests collective entrainment was an important transport phenomenon in our experiments for the smaller grain sizes, likely due to bed impacts by larger grains. Poisson distribution fits to flux histograms for the largest grain size classes suggests collective entrainment was not an important

transport mechanism. In a more general way, we show that this overall cascading effect from large to smaller grains can be initiated in the birth-death model with an initial input signal of white noise, which could represent the motions of relatively large particles, or a system close to the transport threshold. Despite similarity between our experimental results and the expanded birth-death model, the link made here is conceptual, and substantial work remains.

5   For example, high resolution physical or possibly numerical experiments progressing from uniform to mixtures of several size classes could be used to directly test and examine links between entrainment mechanisms and fluctuations of particle flux. Small flume setups would likely be ideal, and will build directly on previous work (Ancey et al., 2008; Ancey, 2010; Heyman et al., 2014; Lee and Jerolmack, 2018) by better identifying the parameter space for the fluid entrainment rate λ_j, the rate constant of particle deposition σ_j and the rate constant of collective entrainment for sediment mixtures μ_{jj}. Furthermore,

10   particle deposition is a key factor in the transport problem and the birth-death formulation, because it contributes directly to the gain of a low pass filter which modulates the flux signal of differing grain sizes. However, our current understanding of particle deposition mechanics is insufficient to precisely quantify this effect in the experiments.

Code and data availability.   The data and Jupyter Notebooks constructed to explore the three particle size birth-death model developed and proposed here, as well as analyze and compile the experimental results can be freely accessed at: https://doi.org/10.6084/m9.figshare.12268727

15   (Chartrand et al., 2020).

Video supplement.   We provide two supplemental videos for download which illustrate sediment transport during a preliminary test experiment (Chartrand, 2017). The video options are at 6 Hz and 150 Hz, compared to the raw video collected at 30 Hz. The videos are useful for two reasons. First, the videos illustrate the general intensity and character of sediment transport discussed and reported here. Second, a collective entrainment event is captured and illustrated by both videos. The collective entrainment event represents a sequence of particle

20   position adjustments which ultimately leads to a short term spike in local particle activity. Beginning at time ∼3 s of the 6 Hz video, the position of a large green particle in the frame center adjusts either due to fluid driven momentum delivery, or a particle collision that is difficult to make out due to depth of field limitations. This initial particle position adjustment leads to a small short term increase in local particle activity. At time ∼25 s, position adjustment of the same large green particle begins again, and about 15 s later a collective entrainment event begins, and there is a larger local short term increase of the local particle activity. The collective entrainment events are interesting because

25   it is not clear if they are due to fluid driven phenomenon, or particle collisions. It is difficult to tell.

Appendix A: Average particle count

The average particle count for each time series was calculated for different aggregation intervals (Figs. A1 and A2). In general, particle sizes smaller than 8 mm exhibit averages that vary among the different aggregation intervals, tending to steady values by the end of each time series. Grain sizes coarser than 8 mm, on the other hand, exhibit approximate steadiness across all

30   aggregation intervals. Differences between the grain sizes in terms of the temporal trends of the aggregated average particle
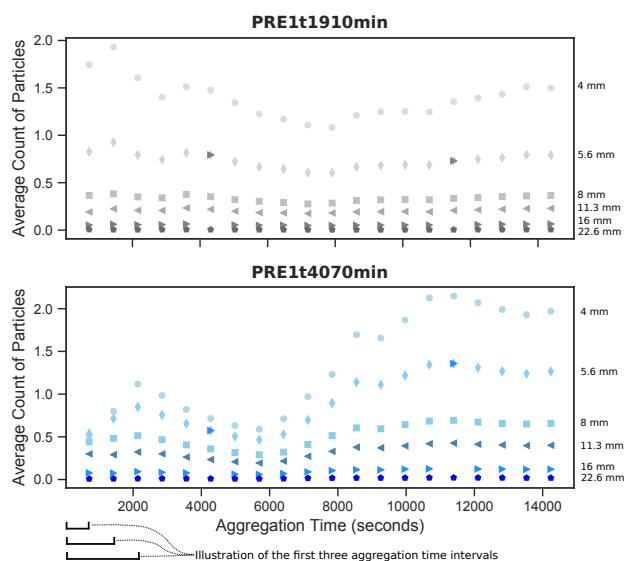
Figure A1. Average fractional flux as particle counts for different aggregation times for steady-state conditions.
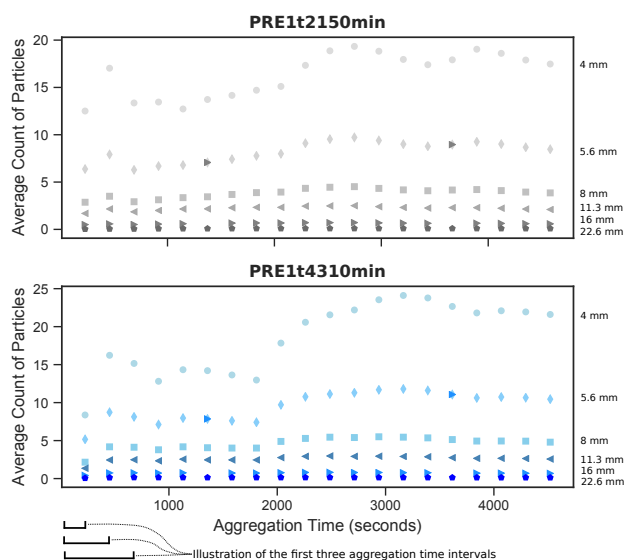

Figure A2. Average fractional flux as particle counts for different aggregation times for transient conditions

counts indicates the finer classes are more responsive to short term changes in particle activity, compared to the coarser grain sizes.

Earth **Surface**
Dynamics
Discussions
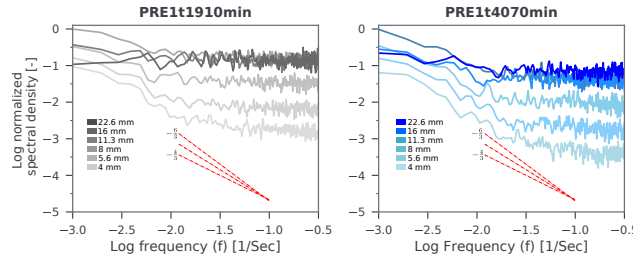
Figure B1. Estimated power spectral density by grain size class for the steady-state time series of mass converted sediment flux, normalized by the maximum power of the 11.3 mm grain size class (t1910) and the 16 mm grain size class (t4070). The dashed red lines provide reference lines of different slope.
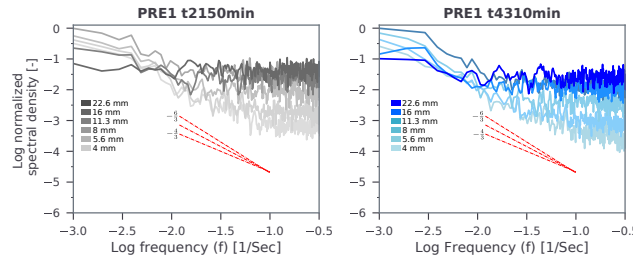
Figure B2. Estimated power spectral density by grain size class for the transient time series of mass converted sediment flux, normalized by the maximum power of the 11.3 mm grain size class (t2150 and t4310). The dashed red lines provide reference lines of different slope.

Appendix B: Power Spectral Density for mass-based flux

The power spectral density for mass-based flux of PRE1 was calculated for all grain sizes and time series following the steps discussed above in Section 3.3 (Figs. B1 and B2). The mass-based power spectral density for each time series indicates that the 11.3 or 16 mm grain size classes have the largest spectral power. Overall, spectra structure is similar to that discussed for the count-based power spectra (Figs. 12 and 13). The finer grain size classes exhibit spectra that decrease exponentially with increasing frequency proportional to $1/f^{-\frac{6}{3}}$ to $1/f^{-\frac{4}{3}}$. The spectra fall off slopes diminish and approach white noise as grain sizes increase to the limiting maximum grain size. The primary difference between the mass-based and count-based spectral densities is the distribution of power among the grain size classes.

Appendix C: Composite Power Spectral Density for particle-based flux

The power spectral density for the particle-based flux summed across all six grain size classes of PRE1 was calculated for the transient time series following the steps discussed above in Section 3.3 (Fig. C1). The composite spectral density structure exhibits power that decreases exponentially with increasing frequency proportional to $1/f^{-\frac{6}{3}}$ to $1/f^{-\frac{4}{3}}$, similar to that discussed for the count-based power spectra finer grain size classes (Figs. 12 and 13).

Earth **Surface**
Dynamics
Discussions
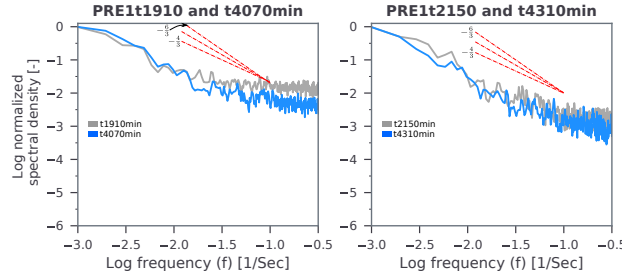
Figure C1. Estimated power spectral density for the total particle flux across all grain sizes for both the steady-state (t1910 and t4070) and transient (t2150 and t4310) time series. Each spectral density distribution has been normalized by the maximum power of the distribution. The dashed red lines provide reference lines of different slope.

Appendix D: Power Spectra of the number of moving particles

The number of active particles n_j of size class j for a specified streambed area A may be expressed as (Ancey, 2010):

$$\frac{\partial n_j(t)}{\partial t} = v_j(t) + \lambda_j(t) + \mu_j n_j(t) - \sigma_j n_j(t) - w_j n_j(t) \tag{D1}$$

The variable v_j is the immigration rate, λ_j is the individual entrainment rate commonly attributed to fluid forces, μ_j is a rate

5   constant of collective entrainment, σ_j is a rate constant of deposition, and w_j is a rate constant of emigration. The Fourier transform for the left hand side of Eq. D1 is found by differentiating the inverse transform with respect to t. Begin with the inverse Fourier transform:

$$f(t) = \frac{1}{2\pi} \int_{-\infty}^{\infty} F(\omega) e^{i\omega t} \partial\omega \tag{D2}$$

Differentiate both sides with respect to t:

10   $$\frac{\partial f(t)}{\partial t} = \frac{1}{2\pi} \frac{\partial}{\partial t} \int_{-\infty}^{\infty} F(\omega) e^{i\omega t} \partial\omega \tag{D3}$$

The derivative on the right hand side is moved inside the integral because it operates on the exponential:

$$f'(t) = \frac{1}{2\pi} \int_{-\infty}^{\infty} F(\omega) \frac{\partial}{\partial t}[e^{i\omega t}] \partial\omega = \frac{1}{2\pi} \int_{-\infty}^{\infty} i\omega F(\omega) e^{i\omega t} \partial\omega \tag{D4}$$

Therefore,

$$f'(t) = \mathcal{F}^{-1}[i\omega F(\omega)], \tag{D5}$$

15   and, we recover the well known result

$$\mathcal{F}[f'(t)] = i\omega F(\omega). \tag{D6}$$

We apply this result to the left hand side of Eq. D1, let a circumflex denote a Fourier transform, and ignore the (ω) dependence for brevity:

$$i\omega\hat{n}_j = \hat{\lambda}_j + \mu_j\hat{n}_j - \sigma_j\hat{n}_j, \tag{D7}$$

where $\omega = 2\pi/T$ is the angular frequency with period T, and we have assumed that $\hat{\nu}_j \approx \hat{w}_j\hat{n}_j$ for adjacent areas of the

5 streambed A under statistically uniform transport. Rearranging,

$$\hat{n}_j = \frac{1}{\sigma_j - \mu_j + i\omega}\hat{\lambda}_j. \tag{D8}$$

We specify $\mathcal{A} = \sigma - \mu$, and we write Eq. D8 in terms of its real and imaginary parts:

$$\hat{n}_j = \frac{1}{\mathcal{A} + i\omega}\hat{\lambda}_j \tag{D9a}$$

$$\hat{n}_j = \left[\frac{1}{\mathcal{A} + i\omega}\frac{(\mathcal{A} - i\omega)}{(\mathcal{A} - i\omega)}\right]\hat{\lambda}_j = \left[\frac{\mathcal{A} - i\omega}{\mathcal{A}^2 + \omega^2}\right]\hat{\lambda}_j \tag{D9b}$$

10 $$\hat{n}_j = \left[\frac{\mathcal{A}}{\mathcal{A}^2 + \omega^2} - i\frac{\omega}{\mathcal{A}^2 + \omega^2}\right]\hat{\lambda}_j \tag{D9c}$$

The magnitude of the active number of particles in motion over A is:

$$|\hat{n}_j| = \left[\frac{\mathcal{A}^2}{(\mathcal{A}^2 + \omega^2)^2} + \frac{\omega^2}{(\mathcal{A}^2 + \omega^2)^2}\right]^{0.5}|\hat{\lambda}_j|, \tag{D10a}$$

$$|\hat{n}_j| = \left[\frac{\mathcal{A}^2 + \omega^2}{(\mathcal{A}^2 + \omega^2)^2}\right]^{0.5}|\hat{\lambda}_j|, \tag{D10b}$$

$$|\hat{n}_j| = \left[\frac{1}{(\mathcal{A}^2 + \omega^2)}\right]^{0.5}|\hat{\lambda}_j|. \tag{D10c}$$

15 Using the definition of $\mathcal{A}$, and noting that $|\hat{n}_j|$ and $|\hat{\lambda}_j|$ are just the signal amplitudes:

$$\hat{n}_j = \frac{1}{\sqrt{(\sigma_j - \mu_j)^2 + \omega^2}}\hat{\lambda}_j. \tag{D11}$$

20

References

Ancey, C.: Stochastic modeling in sediment dynamics: Exner equation for planar bed incipient bed load transport conditions, Journal of Geophysical Research: Earth Surface, 115, https://doi.org/10.1029/2009JF001260, 2010.

Ancey, C. and Heyman, J.: A microstructural approach to bed load transport: mean behaviour and fluctuations of particle transport rates, Journal of Fluid Mechanics, 744, 129–168, https://doi.org/10.1017/jfm.2014.74, 2014.

Ancey, C. and Pascal, I.: Estimating Mean Bedload Transport Rates and Their Uncertainty, Journal of Geophysical Research: Earth Surface, 125, e2020JF005 534, https://doi.org/https://doi.org/10.1029/2020JF005534, 2020.

Ancey, C., Böhm, T., Jodeau, M., and Frey, P.: Statistical description of sediment transport experiments, Physical Review E, 74, 11 302, https://doi.org/10.1103/PhysRevE.74.011302, 2006.

Ancey, C., Davison, A. C., Böhm, T., Jodeau, M., and Frey, P.: Entrainment and motion of coarse particles in a shallow water stream down a steep slope, Journal of Fluid Mechanics, 595, 83–114, https://doi.org/10.1017/S0022112007008774, 2008.

Böhm, T., Ancey, C., Frey, P., Reboud, J.-L., and Ducottet, C.: Fluctuations of the solid discharge of gravity-driven particle flows in a turbulent stream, Phys. Rev. E, 69, 61 307, https://doi.org/10.1103/PhysRevE.69.061307, 2004.

Box, G. E. P., Jenkins, G. M., and Reinsel, G. C.: Time series analysis: Forecasting and control. 4. ed, Hoboken, NJ: Wiley: Wiley, Hoboken, NJ, 2008.

Bunte, K., Abt, S., Potyondy, J., and Sandra, R.: Measurement of Coarse Gravel and Cobble Transport Using Portable Bedload Traps, Journal of Hydraulic Engineering, 130, 879–893, https://doi.org/10.1061/(ASCE)0733-9429(2004)130:9(879), 2004.

Carling, P. A.: Subaqueous gravel dunes, Journal of Sedimentary Research, 69, 534–545, https://doi.org/10.2110/jsr.69.534, 1999.

Chartrand, S.: Gravel mixture sediment transport videos from a straight-walled flume, https://doi.org/dx.doi.org/10.17632/4z7fspfcpv.1, 2017.

Chartrand, S., Jellinek, A., Hassan, M., and Ferrer-Boix, C.: Experimental data set for morphodyanmics of a width-variable gravel-bed stream: new insights on pool-riffle formation, Mendeley Data, https://doi.org/dx.doi.org/10.17632/zmjvt32gj3.3, 2017.

Chartrand, S., Furbish, D. J., and Hassan, M. A.: Experimental sediment transport data using a light table device and analysis code, https://doi.org/10.6084/m9.figshare.12268727.v4, 2020.

Chartrand, S. M., Jellinek, A. M., Hassan, M. A., and Ferrer-Boix, C.: Morphodynamics of a Width-Variable Gravel Bed Stream: New Insights on Pool-Riffle Formation From Physical Experiments, Journal of Geophysical Research: Earth Surface, 123, 2735–2766, https://doi.org/10.1029/2017JF004533, 2018.

Chartrand, S. M., Jellinek, A. M., Hassan, M. A., and Ferrer-Boix, C.: What controls the disequilibrium state of gravel-bed rivers?, Earth Surface Processes and Landforms, 44, 3020–3041, https://doi.org/10.1002/esp.4695, 2019.

Dhont, B. and Ancey, C.: Are Bedload Transport Pulses in Gravel Bed Rivers Created by Bar Migration or Sediment Waves?, Geophysical Research Letters, 45, 5501–5508, https://doi.org/10.1029/2018GL077792, 2018.

Diplas, P., Kuhnle, R., Gray, J., Glysson, D., and Edwards, T.: Sediment transport measurements: Chapter 5, in: Sedimentation engineering: processes, measurements, modeling, and practice, edited by García, M. H., pp. 307–353, American Society of Civil Engineers, https://doi.org/10.1061/9780784408148.ch05, 2008.

Drake, T. G., Shreve, R. L., Dietrich, W. E., Whiting, P. J., and Leopold, L. B.: Bedload transport of fine gravel observed by motion-picture photography, Journal of Fluid Mechanics, 192, 193–217, 1988.

Einstein, H.: Bedload transport as a probability problem, Ph.D. thesis, Mitt. Versuchsanst. fuer Wasserbau, an der Eidg. Techn. Hochschule, Zurich, Switzerland, 1937.

Einstein, H. A.: The Bed-load Function for Sediment Transportation in Open Channel Flows, USDA Soil Conservation Service Technical Bulletin 1026, U.S. Department of Agriculture, 1950.

5 Fathel, S. L., Furbish, D. J., and Schmeeckle, M. W.: Experimental evidence of statistical ensemble behavior in bed load sediment transport, Journal of Geophysical Research: Earth Surface, 120, 2298–2317, https://doi.org/10.1002/2015JF003552, 2015.

Ferrer-Boix, C. and Hassan, M. A.: Channel adjustments to a succession of water pulses in gravel bed rivers, Water Resources Research, 51, 8773–8790, https://doi.org/10.1002/2015WR017664, 2015.

Frey, P., Ducottet, C., and Jay, J.: Fluctuations of bed load solid discharge and grain size distribution on steep slopes with image analysis, 10 Journal of Experimental Fluids, 35, 589–597, https://doi.org/10.1007/s00348-003-0707-9, 2003.

Furbish, D. J., Haff, P. K., Roseberry, J. C., and Schmeeckle, M. W.: A probabilistic description of the bed load sediment flux: 1. Theory, Journal of Geophysical Research: Earth Surface, 117, F03 031, https://doi.org/10.1029/2012JF002352, 2012a.

Furbish, D. J., Roseberry, J. C., and Schmeeckle, M. W.: A probabilistic description of the bed load sediment flux: 3. The particle velocity distribution and the diffusive flux, Journal of Geophysical Research: Earth Surface, 117, F03 033, https://doi.org/10.1029/2012JF002355, 15 2012b.

Furbish, D. J., Schmeeckle, M. W., Schumer, R., and Fathel, S. L.: Probability distributions of bed load particle velocities, accelerations, hop distances, and travel times informed by Jaynes's principle of maximum entropy, Journal of Geophysical Research: Earth Surface, 121, 1373–1390, https://doi.org/10.1002/2016JF003833, 2016.

Furbish, D. J., Fathel, S. L., and Schmeeckle, M. L.: Particle Motions and Bedload Theory: The Entrainment Forms of the Flux and the Exner 20 Equation, in: Gravel-bed rivers, chap. 4, pp. 97–120, Wiley-Blackwell, https://doi.org/10.1002/9781118971437.ch4, 2017.

Goswami, A., Choudhury, G., and Kr. Sarmah, H.: Contributions of Russian Mathematicians in the Development of Probability: A Historical Search, International Journal of Statistics and Systems, pp. 1–27, 2019.

Hassan, M. A., Church, M., and Schick, A. P.: Distance of movement of coarse particles in gravel bed streams, Water Resources Research, 27, 503–511, https://doi.org/10.1029/90WR02762, 1991.

25 Hassan, M. A., Church, M., Lisle, T. E., Brardinoni, F., Benda, L., and Grant, G. E.: Sediment transport and channel morphology of small, forested streams, JAWRA Journal of the American Water Resources Association, 41, 853–876, https://doi.org/10.1111/j.1752-1688.2005.tb03774.x, 2005.

Helley, E. J. and Smith, W.: Development and calibration of a pressure-difference bedload sampler, Tech. rep., United States Geological Survey, https://doi.org/10.3133/ofr73108, 1971.

30 Heyman, J.: A study of the spatio-temporal behaviour of bed load transport rate fluctuations, Ph.D. thesis, Ecole Polytechnique Federale de Lausanne, 2014.

Heyman, J., Mettra, F., Ma, H. B., and Ancey, C.: Statistics of bedload transport over steep slopes: Separation of time scales and collective motion, Geophysical Research Letters, 40, 128–133, https://doi.org/10.1029/2012GL054280, 2013.

Heyman, J., Ma, H. B., Mettra, F., and Ancey, C.: Spatial correlations in bed load transport: Evidence, importance, and modeling, Journal of 35 Geophysical Research F: Earth Surface, 119, 1751–1767, https://doi.org/10.1002/2013JF003003, 2014.

Hubbell, D. W.: Apparatus and techniques for measuring bedload, Tech. rep., United States Geological Survery, https://doi.org/10.3133/wsp1748, 1964.

Hubbell, D. W. and Sayre, W. W.: Sand transport studies with radioactive tracers, Journal of the Hydraulics Division90, 90, 39–68, 1964.

Iseya, F. and Ikeda, H.: Pulsations in bedload transport rates induced by a longitudinal sediment sorting: a flume study using sand and gravel mixtures, Geografiska annaler. Series A. Physical geography, 69, 15–27, 1987.

Jackson, W. L. and Beschta, R. L.: A model of two-phase bedload transport in an oregon coast range stream, Earth Surface Processes and Landforms, 7, 517–527, https://doi.org/10.1002/esp.3290070602, 1982.

5 Jerolmack, D. J. and Paola, C.: Shredding of environmental signals by sediment transport, Geophysical Research Letters, 37, n/a—-n/a, https://doi.org/10.1029/2010GL044638, 2010.

Jones, E., Oliphant, T., Peterson, P., and Others: SciPy: Open source scientific tools for Python, 2001.

Kuhnle, R. A. and Southard, J. B.: Bed load transport fluctuations in a gravel bed laboratory channel, Water Resources Research, 24, 247–260, https://doi.org/10.1029/WR024i002p00247, 1988.

10 Lajeunesse, E., Malverti, L., and Charru, F.: Bed load transport in turbulent flow at the grain scale: Experiments and modeling, Journal of Geophysical Research: Earth Surface, 115, https://doi.org/10.1029/2009JF001628, 2010.

Lee, D. B. and Jerolmack, D.: Determining the scales of collective entrainment in collision-driven bed load, Earth Surface Dynamics, 6, 1089–1099, https://doi.org/10.5194/esurf-6-1089-2018, 2018.

Masteller, C. C. and Finnegan, N. J.: Interplay between grain protrusion and sediment entrainment in an experimental flume, Journal of

15 Geophysical Research: Earth Surface, 122, 274–289, https://doi.org/10.1002/2016JF003943, 2017.

Masteller, C. C., Finnegan, N. J., Turowski, J. M., Yager, E. M., and Rickenmann, D.: History-Dependent Threshold for Motion Revealed by Continuous Bedload Transport Measurements in a Steep Mountain Stream, Geophysical Research Letters, 46, 2583–2591, https://doi.org/10.1029/2018GL081325, 2019.

Meyer-Peter, E. and Muller, R.: Formulas for bed-load transport, in: 2nd Congress International Association of Hydraulic Research

20 (I.A.H.R.), Stockholm, 1948.

Parker, G.: Surface-based bedload transport relation for gravel rivers, Journal of Hydraulic Research, 28, 417–436, https://doi.org/10.1080/00221689009499058, 1990.

Phillips, C. B., Hill, K. M., Paola, C., Singer, M. B., and Jerolmack, D. J.: Effect of Flood Hydrograph Duration, Magnitude, and Shape on Bed Load Transport Dynamics, Geophysical Research Letters, 45, 8264–8271, https://doi.org/10.1029/2018GL078976, 2018.

25 Powell, D. M.: Patterns and Processes of Sediment Sorting in Gravel-Bed Rivers, Progress in Physical Geography, 22, 1–32, https://doi.org/10.1177/030913339802200101, 1998.

Redolfi, M., Bertoldi, W., Tubino, M., and Welber, M.: Bed Load Variability and Morphology of Gravel Bed Rivers Subject to Unsteady Flow: A Laboratory Investigation, Water Resources Research, 54, 842–862, https://doi.org/10.1002/2017WR021143, 2018.

Rickenmann, D.: Variability of Bed Load Transport During Six Summers of Continuous Measurements in Two Austrian Mountain Streams

30 (Fischbach and Ruetz), Water Resources Research, 54, 107–131, https://doi.org/10.1002/2017WR021376, 2018.

Roseberry, J. C., Schmeeckle, M. W., and Furbish, D. J.: A probabilistic description of the bed load sediment flux: 2. Particle activity and motions, Journal of Geophysical Research: Earth Surface, 117, n/a–n/a, https://doi.org/10.1029/2012JF002353, 2012.

Saletti, M., Molnar, P., Zimmermann, A., Hassan, M. A., and Church, M.: Temporal variability and memory in sediment transport in an experimental step-pool channel, Water Resources Research, 51, 9325–9337, https://doi.org/10.1002/2015WR016929, 2015.

35 Shields, A.: Anwendung der Aehnlichkeitsmechanik und der Turbulenzforschung auf die Geschiebebewegung, Mitteilungen der Preußischen Versuchsanstalt f€ur Wasser- bau und Schiffbau, 26, 26 pp., 1936.

Singh, A., Fienberg, K., Jerolmack, D. J., Marr, J., and Foufoula-Georgiou, E.: Experimental evidence for statistical scaling and intermittency in sediment transport rates, Journal of Geophysical Research: Earth Surface, 114, https://doi.org/10.1029/2007JF000963, 2009.

Turowski, J. M., Badoux, A., and Rickenmann, D.: Start and end of bedload transport in gravel-bed streams, Geophysical Research Letters, 38, 5, https://doi.org/10.1029/2010GL046558, 2011.

Whiting, P. J., Dietrich, W. E., Leopold, L. B., Drake, T. G., and Shreve, R. L.: Bedload sheets in heterogeneous sediment, Geology, 16, 105–108, https://doi.org/10.1130/0091-7613(1988)016, 1988.

5 Wiberg, P. L. and Smith, J. D.: Calculations of the critical shear stress for motion of uniform and heterogeneous sediments, Water Resources Research, 23, 1471–1480, https://doi.org/198710.1029/WR023i008p01471, 1987.

Wilcock, P. R. and Crowe, J. C.: Surface-based transport model for mixed-size sediment, Journal of Hydraulic Engineering, 129, 120–128, https://doi.org/10.1061/(ASCE)0733-9429(2003)129:2(120), 2003.

Wilcock, P. R. and McArdell, B. W.: Partial transport of a sand/gravel sediment, Water Resources Research, 33, 235–245,
10 https://doi.org/10.1029/96WR02672, 1997.

Yager, E. M., Schmeeckle, M. W., and Badoux, A.: Resistance Is Not Futile: Grain Resistance Controls on Observed Critical Shields Stress Variations, Journal of Geophysical Research: Earth Surface, 123, 3308–3322, https://doi.org/10.1029/2018JF004817, 2018a.

Yager, E. M., Venditti, J. G., Smith, H. J., and Schmeeckle, M. W.: The trouble with shear stress, Geomorphology, 323, 41–50, https://doi.org/https://doi.org/10.1016/j.geomorph.2018.09.008, 2018b.

15 Zimmermann, A. E., Church, M., and Hassan, M. A.: Video-based gravel transport measurements with a flume mounted light table, Earth Surface Processes and Landforms, 33, 2285–2296, 2008.